Journal of Molecular Graphics and Modelling 81 (2018) 32–49

Contents lists available at ScienceDirect

Journal of Molecular Graphics and Modelling

journal homepage: www.elsevier.com/locate/JMGM

Faster protein folding using enhanced conformational sampling of molecular dynamics simulation

Hiqmet Kamberaj

Department of Computer Engineering, Faculty of Engineering, International Balkan University, Tashko Karadza 11A, Skopje, Republic of Macedonia

ARTICLE INFO

Article history:
Received 23 August 2017
Received in revised form
19 January 2018
Accepted 14 February 2018
Available online 22 February 2018

Keywords:
Protein folding
Enhanced sampling
Molecular dynamics
Swarm particle dynamics

ABSTRACT

In this study, we applied swarm particle-like molecular dynamics (SPMD) approach to enhance conformational sampling of replica exchange simulations. In particular, the approach showed significant improvement in sampling efficiency of conformational phase space when combined with replica exchange method (REM) in computer simulation of peptide/protein folding. First we introduce the augmented dynamical system of equations, and demonstrate the stability of the algorithm. Then, we illustrate the approach by using different fully atomistic and coarse-grained model systems, comparing them with the standard replica exchange method. In addition, we applied SPMD simulation to calculate the time correlation functions of the transitions in a two dimensional surface to demonstrate the enhancement of transition path sampling. Our results showed that folded structure can be obtained in a shorter simulation time using the new method when compared with non-augmented dynamical system. Typically, in less than 0.5 ns using replica exchange runs assuming that native folded structure is known and within simulation time scale of 40 ns in the case of blind structure prediction. Furthermore, the root mean square deviations from the reference structures were less than 2 Å. To demonstrate the performance of new method, we also implemented three simulation protocols using CHARMM software. Comparisons are also performed with standard targeted molecular dynamics simulation method.

1. Introduction

Atomistic molecular dynamics (MD) method now plays a major role in studying macromolecular systems [1] in part because the processes involved at the experimental conditions can largely be governed by the laws of classical statistical mechanics [2]. In particular, it has often been used to study the internal atomic motion [1,3], (poly)peptide and protein folding [4], transition path sampling [5], biomolecular complexes (e.g., protein-DNA, protein-protein and protein-ligand), free energy calculations [6] and protein structure prediction [7]. The main disadvantage of standard MD simulation is the time and size scale limitations of the approach in studying slow conformational motions of complex molecular systems [8,9]. Therefore, the large time and size scale (bio)physical phenomena will indeed require new statistical and computational approaches in order to be studied efficiently [10,11].

Different approaches have been suggested in literature for enhancing the search and sampling efficiency of MD simulations (see the review in Ref. [2]). These approaches are often classified [2] in those that are *smothering or deforming the potential-energy landscape* (e.g., by smothering the energy surface [12–16], using soft-core atoms [13], conformational flooding [17], geometrical constraints [18], or Tsallis-like dynamics [19]), *parallel tempering* (e.g., replica-exchange [20–24], multicanonical algorithms [25], or swarm particle-like dynamics [26–28]), and *coarse-graining* models (e.g., by decreasing number of interaction sites [29–38], or using the so-called collective coordinates [39–41]). These MD methods are often used for exploring conformation transitions (see for example Refs. [42–47]), by enhancing the rate of barrier crossing events either without introducing a bias, or adding bias that can be rigorously removed a posteriori [48]. Long MD simulations (from hundreds of microseconds to milliseconds time scale) have also been achieved by computer engineering using unbiased MD method [49,50], or developing multiple time step integrators, such as reference system propagator algorithm (RESPA) [51–53].

Recently [27] a Swarm Particle-like Molecular Dynamics approach has been presented for use in replica exchange molecular dynamics simulations. The main idea was to allow replicas (representing different system configurations) communicating

E-mail address: h.kamberaj@gmail.com.

https://doi.org/10.1016/j.jmgm.2018.02.008
1093-3263/

with each other through the individual and social knowledge, in addition to considering them as a collection of real particles interacting through the Newtonian forces. The method proved to perform efficiently by optimizing the distribution of replicas among the thermostats with time. In addition, ergodic convergence was observed to be faster without requiring *a priory* knowledge of the energy distribution among the thermostats as a function of temperature. The main advantage of this approach in application with replica exchange simulations is that swarm particle-like dynamics try to pull together the replicas in configuration phase space, increasing in this way the swapping acceptance probability and thus improving the efficiency of algorithm. Moreover, in large due to the individual and social knowledge communications, the swarm replicas cooperatively sample a much larger phase space by steering each other across potential energy barriers.

The equations of motion for a system of g_f degrees of freedom in SPMD approach [27] are similar to the Langevin dynamics [54], and they can be obtained by modifying the Nosé Hamiltonian H_N [55] as given by the time dependent Hamiltonian, $H(t)$:

$$H(t) = H_N + \frac{1}{2}\sum_{j=1}^{g_f}\left[u_1\gamma_1\left(q_j^{\text{Lbest}} - q_j\right)^2 + u_2\gamma_2\left(q_j^{\text{Gbest}} - q_j\right)^2\right] \tag{1}$$

where $\mathbf{q}^{\text{Lbest}}$ represents local best configuration, $\mathbf{q}$, corresponding to the lowest value of the potential energy of system at time t and $\mathbf{q}^{\text{Gbest}}$ represents global best configuration corresponding to the lowest possible value of the potential energy. u_1 and u_2 are two independently uniformly distributed random numbers in the interval $(0, 1)$, and γ_1 and γ_2 are scaling factors which are determined as in Ref. [27]. The second term represents the time-dependent bias energy added in order to augment the dynamics of the system. This is equivalent to coupling of each system's particle to a random force, which excessively increases the kinetic energy of the particle, removed then by the frictional dissipation through the momentum-dependent force as it will be shown in the Theory Section. Bias energy term increases the probability of reaching global minimum state faster and decreasing the amount of time spent in locally stable minimum states has the effect of distorting the Maxwell-Boltzmann distribution of equilibrium system [27] (and the references therein), and therefore, proper re-weighting of the biased trajectory to recover the kinetic properties of the real system is particularly important.

In this study, we will modify the equations of motion introduced in the previous study [27] in order to maintain the Maxwell-Boltzmann distribution of equilibrium for augmented dynamical system. This has the advantage that allows generating simple schemes of the re-weighting technique to calculate the Boltzmann weights of the original dynamical system at a required temperature T, for example, using the Weighted Histogram Analysis Method (WHAM) [48,56], removing both the bias in temperature and energy when combined with replica exchange method. In addition, it is preserving the detailed balance condition when approach is combined with replica exchange method, which requires that

$$T_{i\to j}P_i = T_{j\to i}P_j \tag{2}$$

where $T_{i\to j}$ is the transition probability from the state i (state of replica 1 coupled to inverse temperature β_1 and 2 coupled to β_2) to state j (state of replica 1 coupled to inverse temperature β_2 and 2 coupled to β_1), and P_i is the (quasi) equilibrium probability of finding the system at a state i. Here, probability P_i is sampled using the biased potential. Thus, the acceptance probability of the swapping two neighboring replicas, 1 and 2, assuming that they represent independent simulations, is given by:

$$p_{\text{acc}} = \frac{T_{i\to j}}{T_{j\to i}} = \exp(-(\beta_2 - \beta_1)(U_{\text{bias}}(1) - U_{\text{bias}}(2))) \tag{3}$$

where U_{bias} is the bias potential energy of every replica, given as

$$U_{\text{bias}} = U(\mathbf{q}) + \frac{1}{2}\sum_{j=1}^{g_f}\left[u_1\gamma_1\left(q_j^{\text{Lbest}} - q_j\right)^2 + u_2\gamma_2\left(q_j^{\text{Gbest}} - q_j\right)^2\right] \tag{4}$$

where $U(\mathbf{q})$ is the real potential energy function.

In this study, we will also present a generalization of the method to any generalized collective coordinates by using the projection operator. In addition, we present a weighting technique for calculation of ensemble averages from SPMD simulation. We validated our method by a straightforward comparison between SPMD and standard MD simulations of different test systems, which are characterized by specific structure complexity. We concerned ourselves with a difficult problem in standard MD simulations, such as (poly)peptide and protein folding [57–59]. In addition, comparisons will be performed with standard targeted molecular dynamics simulation [60,61]. In this study, we modeled the biomolecular systems either at coarse-grained or fully atomistic level. The new method is also implemented in CHARMM program [62] in order to increase usability of the technique to a broader range of applications and systems. On the other hand, for the coarse-grained simulations, we employed our in-house C++ code [27], which is designed to perform replica exchange simulations using Nosé-Hoover chain of thermostats approach by coupling each system's degree of freedom to a heat bath. Multiple time-step integrator is used to integrate thermostats degrees of freedom. In both cases, the algorithm of swapping acceptance probability is given by a Metropolis scheme:

$$p_{\text{acc}}(i\leftrightarrow j) = \min\{1, \exp(-(\beta_2 - \beta_1)(U_{\text{bias}}(1) - U_{\text{bias}}(2)))\}$$

Hence, it satisfies the detailed balance condition.

Note that this study is on the spirit of recent attempts [63] of using accelerated molecular dynamics techniques to simulate fast protein folding in explicit solvent environment and different force fields. However, the main aim of our study is to investigate how short the simulation time could be for which protein folding can be obtained, and furthermore, to demonstrate efficiency of the method when combined with replica exchange approach in assessing the speed of protein folding problems using augmented dynamical system. In addition, we will apply SPMD simulation to calculate the time correlation functions of the transitions in a two dimensional surface to demonstrate the enhancement of transition path sampling.

2. Theory

2.1. Swarm particle-like molecular dynamics

For a system of g_f degrees of freedom with masses m_i ($i = 1, \cdots, g_f$), coordinates $\mathbf{q} = (q_1, \cdots, q_{g_f})$, and conjugated momenta $\mathbf{p} = (p_1, \cdots, p_{g_f})$, the Nosé-Hoover dynamics [55,64] of the system coupled to a chain of thermostats [65] is defined in terms of the following equations of motion (for $i = 1, 2, \cdots, g_f$):

$$\begin{aligned}
\dot{q}_i &= \frac{p_i}{m_i},\\
\dot{p}_i &= F_i - \xi_{i,1}p_i\\
\dot{s}_{i,k} &= \xi_{i,k}, \quad \text{for } k = 1,\ 2,\ \cdots,\ M\\
\dot{\xi}_{i,k} &= \frac{G_{i,k}}{Q_{i,k}} - \xi_{i,k+1}\xi_{i,k}, \quad \text{for } k = 1,\ 2,\ \cdots,\ M-1\\
\dot{\xi}_{i,M} &= \frac{G_{i,M}}{Q_{i,M}},
\end{aligned} \tag{5}$$

where M is the length of the Nosé-Hoover chain of thermostats, $\xi_{i,k}$ and $s_{i,k}$ are the thermostat velocities and coordinates, respectively, $(k = 1, \cdots, M)$ associated with temperature T, coupled to ith degrees of freedom. The thermostat forces $G_{i,k}$ are given by

$$G_{i,1} = \frac{p_i^2}{m_i} - k_B T, G_{i,k} = Q_{i,k-1}\left(\xi_{i,k-1}\right)^2 - k_B T \tag{6}$$

for $(k = 2, \cdots, M)$. Here, k_B is the Boltzmann constant, and $Q_{i,k}$ is the thermostat mass (with an optimal choice as in Refs. [55,65]).

To augment the dynamics and to enhance the conformational sampling among the replicas, a new method has been proposed [27] based on the swarm particle-like dynamics. The idea behind this approach is to consider in the system, in addition to the real physical interaction forces between particles, a random force that adds on the momentum a randomness due to the *individual* and *global* knowledge, in a way similar to Langevin dynamics [54], which has been used to increase the cooperative behavior of swarm particles (which in our approach would represent configurations of the system at different instances of time and/or replicas in replica exchange method). Bias energy term has the effect of distorting the Maxwell-Boltzmann distribution of equilibrium system [27]. Therefore, in this study, we will modify the equations of motion introduced previously [27] in order to maintain the Maxwell-Boltzmann distribution of equilibrium for augmented dynamical system.

In particular, we rewrite the MD equations of motion by including the randomness along every generalized collective coordinate as the following (for $i = 1,\ 2,\ \cdots,\ g_f$):

$$\begin{aligned}
\dot{q}_i &= \frac{p_i}{m_i},\\
\dot{q}_i^{\text{Lbest}} &= \frac{p_i^{\text{Lbest}}}{m_i}\delta\left(U(\mathbf{q}) < U\left(\mathbf{q}^{\text{Lbest}}\right)\right),\\
\dot{q}_i^{\text{Gbest}} &= \frac{p_i^{\text{Gbest}}}{m_i}\delta\left(U(\mathbf{q}) < U\left(\mathbf{q}^{\text{Gbest}}\right)\right),\\
\dot{p}_i &= F_i - \xi_{i,1}p_i + \sum_{j=1}^{m} P_{ij}\left(\gamma_1 u_1\left(c_j^{\text{Lbest}} - c_j\right) + \gamma_2 u_2\left(c_j^{\text{Gbest}} - c_j\right)\right)
\end{aligned} \tag{7}$$

$$\begin{aligned}
\dot{p}_i^{\text{Lbest}} &= -\gamma_1 u_1\left(q_i^{\text{Lbest}} - q_i\right) - \xi_{i,1}p_i^{\text{Lbest}}\\
\dot{p}_i^{\text{Gbest}} &= -\gamma_2 u_2\left(q_i^{\text{Gbest}} - q_i\right) - \xi_{i,1}p_i^{\text{Gbest}}\\
\dot{s}_{i,k} &= \xi_{i,k}, \quad \text{for } k = 1,\ 2,\ \cdots,\ M\\
\dot{\xi}_{i,k} &= \frac{G_{i,k}}{Q_{i,k}} - \xi_{i,k+1}\xi_{i,k}, \quad \text{for } k = 1,\ 2,\ \cdots,\ M-1\\
\dot{\xi}_{i,M} &= \frac{G_{i,M}}{Q_{i,M}},
\end{aligned}$$

where $\mathbf{c} = (c_1, c_2, \cdots, c_m)^T$ is the *collective coordinates* vector and $\mathbf{P}$ is the projection operator with m columns corresponding to the $3N$-dimensional unit vectors of transformation from real coordinates $\mathbf{q}$ to collective, $\mathbf{c}$, such that:

$$c_j = \sum_{i=1}^{g_f} P_{ij}q_i$$

In Eq. (7), $\{c_j^{\text{Lbest}}\}_{j=1}^{m}$ represents *local best* collective coordinates corresponding to configuration with the lowest value of the potential energy of the system, which is attempted to be updated at every time step t, and $\{c_j^{\text{Gbest}}\}_{j=1}^{m}$ represents *global best* collective coordinates corresponding to configuration of the final state of the system, or to configuration with the lowest energy among all replicas in the case of replica exchange simulation [66,67]:

$$\begin{aligned}
c_j^{\text{Lbest}} &= \sum_{i=1}^{g_f} P_{ij}q_i^{\text{Lbest}}\\
c_j^{\text{Gbest}} &= \sum_{i=1}^{g_f} P_{ij}q_i^{\text{Gbest}}
\end{aligned}$$

u_1 and u_2 are two independently uniformly distributed random numbers in the interval $(0, 1)$, and γ_1 and γ_2 are scaling factors which are adjusted by trial test runs [27] to ensure the numerical stability of integrators. In Eq. (7), δ corresponds to δ-like function, such that:

$$\delta\left(U(\mathbf{q}) < U\left(\mathbf{q}^{\text{Lbest}}\right)\right) = \begin{cases} 1, & \text{if } U(\mathbf{q}) < U\left(\mathbf{q}^{\text{Lbest}}\right)\\ 0, & \text{otherwise} \end{cases}$$

and

$$\delta\left(U(\mathbf{q}) < U\left(\mathbf{q}^{\text{Gbest}}\right)\right) = \begin{cases} 1, & \text{if } U(\mathbf{q}) < U\left(\mathbf{q}^{\text{Gbest}}\right)\\ 0, & \text{otherwise} \end{cases}$$

Note that the augmented dynamical system, Eq. (7), is characterized by an extended phase space of real variables:

$$\left((q_i, p_i), \left(q_i^{\text{Lbest}}, p_i^{\text{Lbest}}\right), \left(q_i^{\text{Gbest}}, p_i^{\text{Gbest}}\right)\right), \quad i = 1\cdots, g_f$$

and the phase space of thermostats variables is characterized by:

$$(s_{i,k}, \xi_{i,k}), \quad i = 1, \cdots, g_f;\ k = 1, \cdots, M$$

These equations sample an equilibrium canonical distribution in the extended phase space of a *non-physical* system, characterized by the total energy function:

$$
\begin{aligned}
E_{\text{ext}} &= \sum_{i=1}^{g_f} \frac{p_i^2}{2m_i} \\
&+ \left(\sum_{i=1}^{g_f} \frac{\left(p_i^{\text{Lbest}}\right)^2}{2m_i} \right) \delta\left(U(\mathbf{q}) < U\left(\mathbf{q}^{\text{Lbest}}\right)\right) \\
&+ \underbrace{\left(\sum_{i=1}^{g_f} \frac{\left(p_i^{\text{Gbest}}\right)^2}{2m_i} \right) \delta\left(U(\mathbf{q}) < U\left(\mathbf{q}^{\text{Gbest}}\right)\right)}_{E_{\text{tot,kin}}} \\
&\underbrace{+U(\mathbf{q}) + \frac{1}{2}\sum_{j=1}^{g_f} \left[u_1\gamma_1\left(q_j^{\text{Lbest}} - q_j\right)^2 + u_2\gamma_2\left(q_j^{\text{Gbest}} - q_j\right)^2 \right]}_{U_{\text{bias}}} \\
&+ \underbrace{\sum_{i=1}^{g_f}\sum_{k=1}^{M} \left(\frac{Q_{i,k}\xi_{i,k}^2}{2} + k_B T s_{i,k} \right)}_{E_{\text{thermo}}}
\end{aligned}
\tag{8}
$$

which is a constant of motion. In Eq. (8), the sum of the first three terms represents the total kinetic energy, $E_{\text{tot,kin}}$, of non-physical system, the fourth and fifth terms give the total potential energy including bias term, U_{bias}, and the last term represents the thermostat energy, E_{thermo}. In order to obtain the Boltzmann's weights of the equilibrium canonical distribution for the *physical* system, the WHAM can be used [27,48], as explained in the following sections. The main idea of using the non-physical extended variable phase space system is to explore metastable and rare transition events [68] (and the references therein), or to improve the conformation phase space sampling [19,69] (and the references therein). The first bias term in the expression for $\dot{p}_i$ (Eq. (7)) indicates the tendency to steer the system towards the configuration with the best energy that a particular replica has visited at any instant time t, reflecting an enhanced local basin sampling process. On the other hand, the second bias term in the same expression indicates the "information" shared among the replicas and their cooperative behavior which steers them towards the best position (corresponding to the configuration with the lowest value of potential energy function among all replicas) found at any instant time, reflecting an enhancement of barrier crossing rate. Therefore, we can think of our biasing algorithm as a combination of two terms, where the first bias term is acting similarly to the umbrella sampling approach [70,71] and the second bias term behaving similarly to steered molecular dynamics simulation approach [72], or other approaches, such as in targeted molecular dynamics simulation [60,61]. We hope and believe, as it will also demonstrated with some example in the following sections, that the algorithm introduced here represents an augmented dynamical system, enhancing the transition path sampling in phase space. It also represents an efficient sampling method in temperature space, by increasing the swapping probability among the neighboring replicas, which is a common problem in standard replica exchange methods [73–77].

To show that the equations of motion preserve the detailed balance condition, we can start by introducing the probability of observing the trajectories for a whole path in the configuration space assuming that the states form a Markovian chain of states as:

$$
P_k\left(\mathbf{X}_T^k\right) = \exp(-\beta_k E(\mathbf{x}_{k,0})) \prod_{t=0}^{T-1} \pi(\mathbf{x}_{k,t} \to \mathbf{x}_{k,t+1})
$$

where β_k in the inverse temperature of the k-th thermostat and $E(\mathbf{x}_{k,t})$ is the total energy at $\mathbf{x}_{k,t}$, and $\mathbf{X}_T^k$ represents T copies of phase space

$$
\mathbf{X}_T^k = \left\{ \mathbf{x}_{k,0} \to \mathbf{x}_{k,1} \to \cdots \to \mathbf{x}_{k,T-1} \right\}
$$

where $\mathbf{x}_{k,t}$ $(t = 0, 1, \cdots, T-1)$ are points in a $3N$-dimensional phase space. The initial time slice is canonically distributed:

$$
\rho_{init}(\mathbf{x}_{k,0}) = \exp(-\beta_k E(\mathbf{x}_{k,0}))
$$

where $E(\mathbf{x}_{k,0})$ is the initial unbiased energy of the system for k-th replica.

Here, $\pi(\mathbf{x}_{k,t} \to \mathbf{x}_{k,t+1})$ represents the probability of each time step propagation, which depends on the details of deterministic dynamics (or stochastic, such as in Monte Carlo algorithm). Usually, any Markovian transition probability $\pi(\mathbf{x}_{k,t} \to \mathbf{x}_{k,t+1})$ can be chosen, as requirement it should conserve the Boltzmann distribution. In our study, we have proposed as a choice for $\pi(\mathbf{x}_{k,t} \to \mathbf{x}_{k,t+1})$ the action characterized by Eq. (7), which just conserves a Boltzmann distribution of non-physical system. In the case when dynamics are determined by the Newtonian dynamics, then

$$
p(\mathbf{x}_t \to \mathbf{x}_{t+1}) = \delta(\mathbf{x}_{t+1} - \Phi_{\Delta t}(\mathbf{x}_t))
$$

where δ is the delta function and $\Phi_{\Delta t}(\mathbf{x}_t)$ represents a discrete flow map characterizing the numerical integrator for propagation with one time step Δt. Thus, the trajectory can be generated by sampling initial state and propagating using Hamiltonian dynamics, and hence, the flow map is time reversible. In the case when dynamics are governed by Eq. (7), although, the structure is not symplectic, it is time reversible, which can be seen from Eq. (7).

Note that for the equations motion to be time reversible, they should preserve the form when time is reversed $t \to -t$, which can be easily shown using $p(-t) = -p(t)$ and $q(-t) = q(t)$, hence $q^{Lbest}(-t) = q^{Lbest}(t)$ and $q^{Gbest}(-t) = q^{Gbest}(t)$. Moreover, although the dynamical structure is non-Hamiltonian, there are already numerical integrators, employed in all our calculations, which provide time reversible flow maps, i.e., $\Phi_{-\Delta t}(\mathbf{x}_t) = \Phi_{\Delta t}(\mathbf{x}_t)$. Therefore, the condition given by Eq. (2) with probability given as described above, satisfies the detailed balance condition. Moreover, projection operator $\mathbf{P}$ depends on the position fluctuations, as such, it does not violate the time reversibility of structure dynamics.

Note that for the clarity of exposition we are denoting, in this study, the MD simulations with dynamics represented by Eq. (5) as "Standard MD" and replica exchange simulations as in Refs. [66,67] with dynamics governed by Eq. (5) as "REM:MD". In the case when dynamics are governed by Eq. (7), we are going to name the standard MD simulation as "SPMD", and replica exchange simulations as in Refs. [66,67] governed by Eq. (7) as "REM:SPMD".

2.2. Re-weighting of ensemble averages

Modifying Eq. (5) as in Eq. (7) is the same as *adding* energy into the system to increase the probability of reaching global minimum faster and decreasing the amount of time spent in a local metastable minimum [27]. This has the effect of generating the Maxwell-Boltzmann distribution of equilibrium for a non-physical system (see also Ref. [78]), therefore requires re-weighting of the trajectory to recover the kinetic properties and perform ensemble

averages using the Maxwell-Boltzmann distribution of original physical system.

A similar scheme of the re-weighting has been suggested [27] as in Refs. [78,79] used to calculate the Boltzmann weights of the original dynamical system. In this approach, for the numerical analysis, we set up K simulations with initial positions and momenta, $\{(\mathbf{q}_0^{(k)}, \mathbf{p}_0^{(k)})\}_{k=1}^{K}$, from an equilibrium unbiased distribution. For every biased SPMD simulation governed by Eq. (7), frequently at regular time interval, we record system configurations, let say T in total. Then, the ensemble average of any quantity $\mathscr{A}$ is calculated as:

$$\left\langle \mathscr{A} \right\rangle = \frac{\sum_{t=1}^{T}\sum_{k=1}^{K}\mathscr{A}^{(k)}(t)W^{(k)}(t)}{\sum_{t=1}^{T}\sum_{k=1}^{K}W^{(k)}(t)}$$

where $\mathscr{A}^{(k)}(t)$ is the value of $\mathscr{A}$ at time t from the k-th biased simulation and $W^{(k)}(t)$ is the value of biased weight at time t from the k-th simulation defined in Ref. [27]. Note that $W^{(k)}(t)$ includes both, the bias due to different temperatures and the bias due to biasing the potential, therefore, if there is no bias energy term, then it simply considers the bias due to using different temperatures compare to target one for each replica, which is treated as in Ref. [48]. In practice, the summations are performed using the WHAM [27,48].

2.3. Rate constant calculations

The rate constant can be calculated using the microscopic approximation and fluctuation-dissipation theorem from the time correlation function [80].

$$C(t) = \frac{\langle h_A(t_0)h_B(t)\rangle_{t_0}}{\langle h_A(t_0)\rangle_{t_0}} \tag{9}$$

where $\langle\cdots\rangle_{t_0}$ indicates an average over an ensemble of trajectories that are initialized from an equilibrium distribution in the phase space. In Eq. (9), h_A and h_B are the population of states A and B, respectively, given by

$$h_A(t) = \begin{cases} 1 & \text{if } \mathbf{r}(t)\in A \\ 0 & \text{otherwise} \end{cases}, \quad h_B(t) = \begin{cases} 1 & \text{if } \mathbf{r}(t)\in B \\ 0 & \text{otherwise} \end{cases}$$

$C(t)$ describes the probability of finding the system at state B after time t, if it was initially at state A. This probability increases from 0 to $\langle h_B(t)\rangle_{t_0}$ with a time dependence that is exponential after a transient time τ_m, assuming that the two states A and B are separated by a single maximum, which is modeled as:

$$C(t) = a(1 - \exp(-t/\tau))$$

where τ is the transition time ($\tau \gg \tau_m$) and a is a constant. Note that for $\tau_m < t \ll \tau$, we can approximate $C(t)$ as

$$C(t) \approx \frac{a}{\tau}t \equiv k_{A\to B}t \tag{10}$$

$k_{A\to B}$ is the rate constant given by

$$k_{A\to B} = \frac{a}{\tau}$$

The condition $t > \tau_m$ determines the shortest time length for the trajectory to cross a single bottleneck. The trajectories should be long enough to catch the linear growth of the time correlation $C(t)$. All the trajectories collected in this way will form the *transition path ensemble*. If state B is not reached from A in typically one step, but through one or more intermediate states, $C(t)$ will not show linear behavior after a short period of time, which can be used as a fact to discover other intermediate states [80] (and the references therein.)

2.4. Re-weighting of rate constants

The time correlation calculated according to Eq. (9) is related to the exponential of free energy, which is in fact the reversible work involved in confining the phase space trajectories initiated from A to B at time t [79]; that is

$$C(t) = \exp(-\beta\Delta F_{AB}(t))$$

where F_{AB} is the reversible work. Dynamical system characterized by Eq. (7) represents another special time correlation function calculated based on trajectories which involve faster compare to non-augmenting dynamical system characterized by Eq. (5). Adding bias to the original potential energy function will reconstruct a new free-energy profile on the subspace $\Gamma(\mathbf{c})$ extended by the collective coordinates $\mathbf{c}$, which based on the Jarzynski identity [81] is written as [79]:

$$\begin{aligned} C(t) &\equiv \exp(-\beta F'_{AB}(\mathbf{c})) \\ &= \left\langle \delta(\mathbf{c} - \mathbf{c}(\mathbf{\Gamma}(t)))e^{-\beta\left(F_{AB}(t) - \Delta U^{\text{bias}}(\mathbf{c}(\mathbf{\Gamma}(t),t))\right)} \right\rangle \end{aligned} \tag{11}$$

We further can write the time correlation function as:

$$C(t) = \frac{\int d\mathbf{\Gamma}_0 \rho'(\mathbf{q}_0)\rho(\mathbf{p}_0)W(\mathbf{q}_t)h_A(\mathbf{\Gamma}_0)h_B(\mathbf{\Gamma}_t)}{\int d\mathbf{\Gamma}_0 \rho'(\mathbf{q}_0)\rho(\mathbf{p}_0)W(\mathbf{q}_t)h_A(\mathbf{\Gamma}_0)} \tag{12}$$

$$= \frac{\langle W(\mathbf{q}_t)h_A(\mathbf{\Gamma}_0)h_B(\mathbf{\Gamma}_t)\rangle'}{\langle W(\mathbf{q}_t)h_A(\mathbf{\Gamma}_0)\rangle'} \tag{13}$$

where

$$W(\mathbf{q}_t) = \exp\left(\beta\Delta U^{\text{bias}}(\mathbf{q}_t)\right)$$

$\rho'(\mathbf{q}_0)$ is the equilibrium spacial distribution with biased potential energy function and $\rho(\mathbf{p}_0)$ is the equilibrium distribution of the momenta. Here, $\langle\cdots\rangle'$ denotes the ensemble average over the equilibrium distribution with biased potential.

During the numerical analysis, we set up K simulations with initial positions and momenta, $\{(\mathbf{q}_0^{(k)}, \mathbf{p}_0^{(k)})\}_{k=1}^{K}$, from an equilibrium unbiased distribution, where each corresponds to the system being at state A. Then, we started K simulations using these initial conditions with biased potential energy function for a time $t > \tau_m$. For every simulation at any time t, we record whether the system has visited state B or not; if state B was visited, then the accumulator $h_B(t)$ is increased by one, otherwise it remains unchanged. Then, the time correlation function is calculated as:

$$C(t) = \frac{\sum_{k=1}^{K}h_B^{(k)}(t)W^{(k)}(t)}{\sum_{k=1}^{K}W^{(k)}(t)} \tag{14}$$

where $h_B^{(k)}(t)$ is the value of h_B at time t from the k-th simulation and $W^{(k)}(t)$ is the value of biased weight at time t from the k-th simulation.

3. Computational methods

3.1. Coarse-grained model

We considered the coarse-grained model of a protein system. In particular, we considered α-helical (residues 46 to 58) of Bovine Pancreatic Trypsin Inhibitor (PDB ID 5PTI [82]). The potential energy function of this system is defined as [38].

$$\begin{aligned} U(\mathbf{r}_1,\cdots,\mathbf{r}_N) &= \sum_{bonds} k_b(\ell-\ell_0)^2 \\ &+ \sum_{angles} k_{\theta,1}(\theta-\theta_0)^2 + k_{\theta,2}(\theta-\theta_0)^3 + k_{\theta,3}(\theta-\theta_0)^4 \\ &+ \sum_{dihedrals} k_\phi(\phi-\phi_0)^2 \\ &+ \sum_{i=1}^{N_{natives}} \sum_{j,|i-j|>3}^{N_{natives}} \varepsilon_{ij}\left[\left(1-\exp\left(-\alpha\left(r_{ij}-r_{ij}^{min}\right)\right)\right)^2-1\right] \\ &+ \sum_{i=1}^{N_{non-natives}} \sum_{j,|i-j|>3}^{N_{non-natives}} \varepsilon_{ij}\left[\left(1-\exp\left(-\alpha\left(r_{ij}-r_{ij}^{min}\right)\right)\right)^2-1\right] \\ &+ \sum_{i=1}^{N} \sum_{j,|i-j|>3}^{N} \frac{q_iq_j}{4\pi\varepsilon_0\varepsilon} \end{aligned} \tag{15}$$

where ℓ_0, θ_0, and ϕ_0 are the bond length, bending and dihedral angles equilibrium values, respectively. Here, $\ell_0 = 3.8$ Å, θ_0 for different angles are taken from Ref. [38], and ϕ_0 are calculated based on the initial native structure. The force constants are

$$k_b = 70 \text{ kcal mol}^{-1} \text{ Å}^{-2},\ k_\phi = 5 \text{ kcal mol}^{-1} \text{ rad}^{-2}$$

and the force constants for the bending angle are determined as:

$$k_{\theta,1} = \frac{1}{2}k_1$$

$$k_{\theta,2} = -\frac{1}{3(\theta_1-\theta_0)}(2k_1+k_2)$$

$$k_{\theta,3} = \frac{1}{4(\theta_1-\theta_0)^2}(k_1+k_2)$$

where θ_1, θ_0, k_1 and k_2 are given as in Ref. [38]. $N_{natives}$ is the number of native contacts defined whenever the distance between two coarse-grained particles is less or equal to 6.5 Å. All the other contacts are called non-native contacts. The values of ε_{ij} and α for native contacts are, respectively,

$$\varepsilon_{ij} = 6\exp\left(-r_{ij}^{min}/2.8\right),\ \alpha = 0.7$$

and for non-native contacts they are given as

$$\varepsilon_{ij} = 0.20708,\ \alpha = 0.70711$$

For the native contacts r_{ij}^{min} is the distance between two coarse-grained particles from the initial native structure, and for non-native contacts this distance is fixed at $r_{ij}^{min} = 9.75$. The sum of non-bonded interactions runs over all pairs which are separated by at least 3 bonds. Here, q_i and q_j represent the charges of residues. In our coarse-grained model, to Arg, His and Lys a charge of $+1$ is assigned to the coarse-grained particles and, for Asp and Glu a charge of -1 is assigned to the coarse-grained particles. All the other residues have a charge zero. ε represents the dielectric effects of the solvent environment and it has been taken $\varepsilon = 4$.

In this study, we coupled 11 independent replicas with 11 thermostats at different temperatures in the interval from 100 to 600 K distributed according to the geometric progression. We used the first 10^4 steps for equilibration, and collected the data for further 10^6 steps by saving the configuration snapshots every 50 steps. The swapping attempts were performed every 5 time steps, and the integration time step was 5 fs. Here, we used a temperature coupling of the scaling constants, $\gamma_1 = \gamma_2 = 0.2/k_BT$, in order to control the magnitude of bias potential energy among the replicas. In particular, to avoid large distortion from the Maxwell-Boltzmann distribution for high temperature replicas.

3.2. Atomistic models

In this study, we also considered four biomolecular systems described by atomistic models. For these models, SPMD algorithm is implemented in CHARMM software [62] using the package available numerical integrators. In all our simulations we used the implicit model for the solvent with EEF1 force field [83], which combines CHARMM19 force field with an excluded volume implicit solvation model. We used four different systems for testing the method. First system is the B fragment of staphylococcal protein A, which is a sequence of 46 amino acids characterized by three helices, as reported from experimental NMR solution and X-ray crystal data (with PDB ID 1BDD [84]). The other systems include, respectively, an α-helix peptide, which includes residues 46–58 of the bovine pancreatic trypsin inhibitor from experimental X-ray crystal structure (represented by PDB ID 5PTI [82]) and β-sheet peptide, which includes the residues 41–56 of the C2 fragment of streptococcal protein G (PDB ID 1FCC [85]). The last system was the C2 fragment of protein G composed of 56 amino acids as seen from experimental X-ray crystal structure (with PDB ID 1FCC [85]).

All our initial structures were prepared using CHARMM-GUI, a web-based graphical interface for CHARMM [86]. Then, the initial structures were minimized using Conjugated Gradient module of CHARMM for 10000 steps in gas phase by keeping fixed all heavy atoms and allowing the hydrogen atoms moving. Coordinates of the structures obtained at the end of minimization are used as $\mathbf{q}^{\text{Gbest}}$ coordinates, in the case of "Protocol 1″ and "Protocol 2″ described in the "Results and discussion" Section.

EEF1 is setup using the atomic solvation parameters as in Ref. [87] and CHARMM19 force field with specific modifications for non-bonded interactions as implemented in CHARMM [83]. Equilibration continued for 2000 steps of minimization using Steepest Descent method, followed by Conjugated Gradient and Adopted Basis Newton-Raphson methods for another 2000 steps each, allowing now all atoms moving. A heating/cooling task was then setup using velocity Verlet algorithm in CHARMM for 20 ps. Each system was first heated up to 1510 K, starting from 10 K, for 15 ps, then it was cooled down for another 15 ps to 300 K. During this task a completely unfolded structure was generated for each system, which then was further equilibrated for 20 ps at constant $(N;\ V;\ T)$ conditions using Nosé-Hoover chain of thermostats dynamics with chain length $M = 3$, solved numerically using velocity-Verlet integrator [88] (VV2 module in CHARMM [89]). All bonds involving hydrogen were constraint using the SHAKE algorithm [90], and a group based cutoff of 12 Å was used for long-range interactions. A switching function was used for both electrostatic and van der Waals interactions between 11 Å and 12 Å, and a distance dependent dielectric constant was used for solvent. The time step of numerical integration was 2 fs.

We applied three different protocols in the production run for

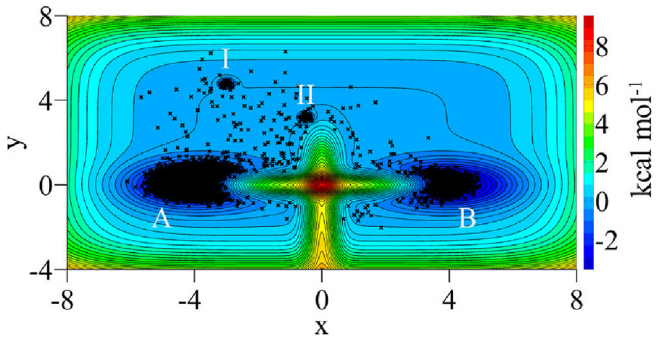

Fig. 1. A two-dimensional colormap of the potential energy function model. The potential is characterized by four minimum states, labeled as *I*, *II*, *A* and *B*. Contour lines correspond to $0.5k_BT$ (in Kcal mol^{-1}). Dotted points represents a few snapshots saved from the SPMD simulation as illustration. Transitions are observed between all minimum states.

each system. In the first protocol, we used a single Nosé-Hoover chain of thermostats at $T = 300$ K, and for $\mathbf{q}^{\text{Gbest}}$ we used the native X-ray crystal structure coordinates after added hydrogen atoms were optimized to their best position by performing an energy minimization, which was fixed at the beginning of simulation for every system studied here.

In the second protocol, a replica exchange simulation was established using ENSEMBLE module in CHARMM, and $\mathbf{q}^{\text{Gbest}}$ were also fixed at the native X-ray crystal structure coordinates at the beginning of simulation for every system (after added hydrogen atoms were optimized to their best position by performing an energy minimization). In our simulations, we employed four replicas for each system investigated here, coupled to four different thermostats kept at temperatures 280 K, 300 K, 320 K, and 340 K, respectively. Trajectories of 1 ns in length are used for data analysis, with coordinates recorded at every 0.4 ps collected from each temperature. In this protocol, only backbone atoms were selected to be biased as in Eq. (7).

In the third protocol, similarly to the second protocol, a replica exchange simulation was employed using ENSEMBLE module in CHARMM, but $\mathbf{q}^{\text{Gbest}}$ were updated every time step corresponding to coordinates of configuration with the lowest value of potential energy among all replicas, performing in this way a blind prediction of protein structure. In this protocol, we doubled the number of replicas and thermostats associated with them to eight, where the thermostats were kept at temperatures 280 K, 300 K, 320 K, 340 K, 360 K, 380 K, 400 K and 420 K, respectively. Trajectories of 40 ns in length are used for data analysis from each temperature, with coordinates recorded at every 2 ps. On the other hand, in this protocol, all heavy atoms were selected to be biased as in Eq. (7).

In all our three simulation protocols, the constants γ_1 and γ_2 were fixed at values 0.01 and 0.1, respectively, after some trial test runs. The configurations of neighboring replicas were swapped regularly at every 100 steps.

4. Results and discussion

4.1. Two dimensional surface model

As the first test model system, we considered a particle moving in a two dimensions spatial space characterized by the following potential function [4] (and the references therein):

$$\begin{aligned} U(x,y) = &-4\exp\left(-\frac{1}{4}(x+4)^2 - y^2\right) \\ &-4\exp\left(-\frac{1}{4}(x-4)^2 - y^2\right) \\ &+\frac{1}{5625}\left(\frac{17}{400}x^6 + \frac{1}{2}(y-2)^6\right) \\ &+5\exp\left(-4x^2 - \frac{1}{100}(y+1)^4\right) \\ &+5\exp\left(-\frac{81}{10000}x^4 - 4y^2\right) \\ &-2\exp\left(-\frac{81}{4}\left((x+3)^2 + \left(y-\frac{24}{5}\right)^2\right)\right) \\ &-2\exp\left(-\frac{81}{4}\left(\left(x+\frac{1}{2}\right)^2 + \left(y-\frac{16}{5}\right)^2\right)\right) \end{aligned} \tag{16}$$

The potential function exhibits four stable minimum states: *A* at point $(-4, 0)$ and *B* at $(4, 0)$, and the intermediate states *I* at point $\left(-3, \frac{24}{5}\right)$ and *II* at point $\left(\frac{1}{2}, \frac{16}{5}\right)$, as shown in Fig. 1. Thus, the two deep minimum states *A* and *B* are connected by one channel, which contains two less pronounced minimum metastable states, *I* and *II*.

In our simulations, the mass of particle moving under the above potential is $m = 1$ amu. The initial position was randomly chosen in a square of side 20 Å with origin of the coordinate system at the center of square, and the initial velocity was chosen according to the Maxwell-Boltzmann distribution at temperature $T = 300$ K. The time step was fixed at $\Delta t = 0.001$ ps. First, we checked the stability of algorithm by monitoring the extended total energy, which is a constant of motion. Initially, we run fixed number of particle *N*,

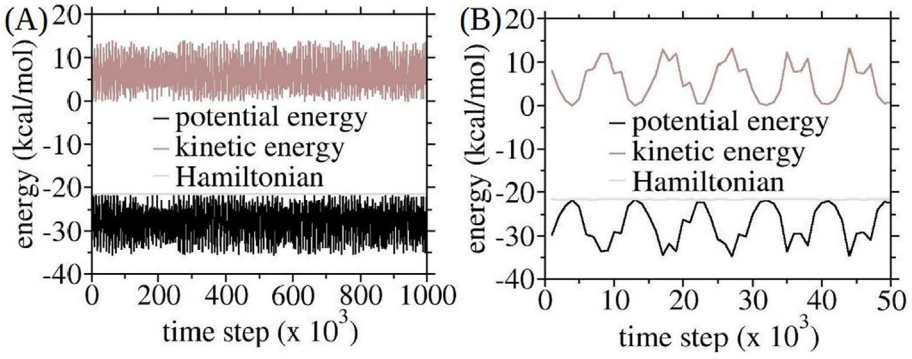

Fig. 2. The trajectory of potential (U_{bias}) and kinetic energy ($E_{\text{tot,kin}}$) of the non-physical system of a particle moving in a two dimensional potential energy surface using *NVE* ensemble with a time step of $\Delta t = 0.001$ ps: (A) Block averages over 1000 blocks and (B) the first 50 blocks. The length of each block is 1000 MD steps.

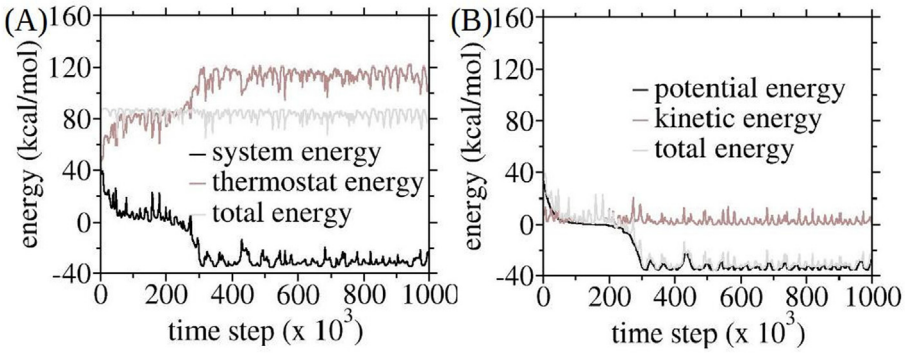

Fig. 3. The trajectory of energy decomposition for the non-physical system, and thermostat total energy for a particle moving in a two dimensional potential energy surface using *NVT* ensemble with a time step of $\Delta t = 0.001$ ps and thermostat chain length of $M = 3$: (A) Block averages over 1000 blocks of $U_{\text{bias}} + E_{\text{tot,kin}}$; (B) Instantaneous values of U_{bias} and $E_{\text{tot,kin}}$. The length of each block is 1000 MD steps.

volume V, and total energy E ensemble simulation, which corresponds to Hamiltonian dynamical system, with total energy (which equals the extended Hamiltonian) of non-physical system given by:

$$H_{\text{ext}} = \sum_{i=1}^{g_f} \frac{p_i^2}{2m_i} + \left(\sum_{i=1}^{g_f} \frac{\left(p_i^{\text{Lbest}}\right)^2}{2m_i} \right) \delta\left(U(\mathbf{q}) < U\left(\mathbf{q}^{\text{Lbest}}\right)\right) + \left(\sum_{i=1}^{g_f} \frac{\left(p_i^{\text{Gbest}}\right)^2}{2m_i} \right) \delta\left(U(\mathbf{q}) < U\left(\mathbf{q}^{\text{Gbest}}\right)\right) + U(\mathbf{q}) + \frac{1}{2}\sum_{j=1}^{g_f} \left[u_1\gamma_1\left(q_j^{\text{Lbest}} - q_j\right)^2 + u_2\gamma_2\left(q_j^{\text{Gbest}} - q_j\right)^2 \right] \tag{17}$$

with $g_f = 2$. H_{ext} represents a constant of motion. H_{ext} as a function of MD time step is shown in Fig. 2(A) using block averages with length of 1000 MD steps. Indeed, our results show that H_{ext} is constant during the course of SPMD simulation run (see also Fig. 2(A)). We also compared the instantaneous fluctuations of the total potential, U_{bias}, and extended kinetic energy of non-physical system, $E_{\text{tot,kin}}$, which are shown in Fig. 2(B). Interestingly, our data indicate that fluctuations of potential and kinetic energy cancel each other yielding a constant total energy.

We also run SPMD simulation at constant N, V and temperature T ensemble, and monitored the trajectory of total extended energy, E_{tot} (see Eq. (8)). It is expected that the fluctuations of total energy, $U_{\text{bias}} + E_{\text{tot,kin}}$, and thermostat energy, E_{thermo}, to cancel each other, such that E_{tot} remains constant during the simulation. Indeed, our results, shown in Fig. 3, indicate that total extended energy, E_{tot}, is a constant of motion. It is worth noting the jump in total energy $U_{\text{bias}} + E_{\text{tot,kin}}$ (see Fig. 3(A)), which indicates a transition to lower energy states. An explanation of this finding is that during this transition an amount of energy is added to system in the form of kinetic energy, expressed by the second and third terms in Eq. (8), which is released to the bath, by increasing E_{thermo}, in order to maintain a constant total energy E_{tot}, keeping in this way temperature of the system equal to target T. This is also demonstrated in Fig. 3(B), which shows trajectories of $E_{\text{tot,kin}}$, U_{bias}, and $U_{\text{bias}} + E_{\text{tot,kin}}$. As expected, our results show that $E_{\text{tot,kin}}$ is constant, and U_{bias} exhibits a transition to a lower value of energy.

In addition, we calculated the probability distribution of projections of particle's velocity along the x and y axes, and compared the results with Maxwell-Boltzmann distribution at target temperature $T = 300$ K. Results are shown graphically in Fig. 4, along with χ^2 and correlation coefficients between the two distributions. It is worth noting that χ^2 values for both projections are small indicating that, with a 95% confidence level, distributions obtained from SPMD data correspond to the Maxwell-Boltzmann, as also expected from our theoretical considerations of dynamics governed by Eq. (7). Moreover, a very high correlation is obtained between

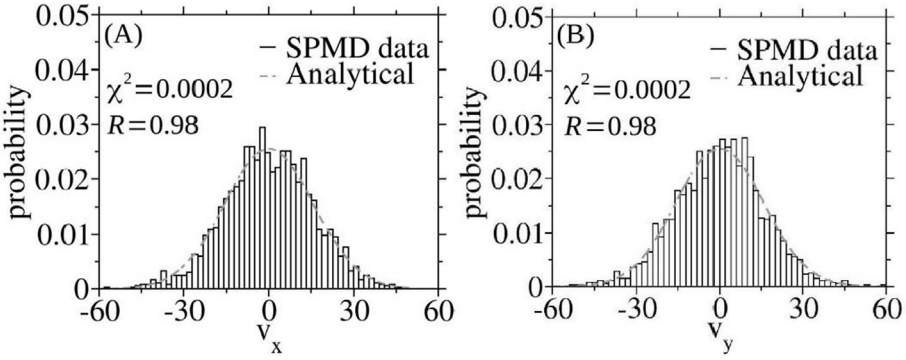

Fig. 4. Probability distribution of particle's velocity projections (A) along x-axis and (B) y-axis using SPMD simulation run for a particle moving in a two dimensional potential energy surface. Dashed lines represent analytical curves calculates using Maxwell-Boltzmann distribution at $T = 300$ K. In addition, the χ^2 and correlation coefficients between the calculated and analytical distributions are shown.

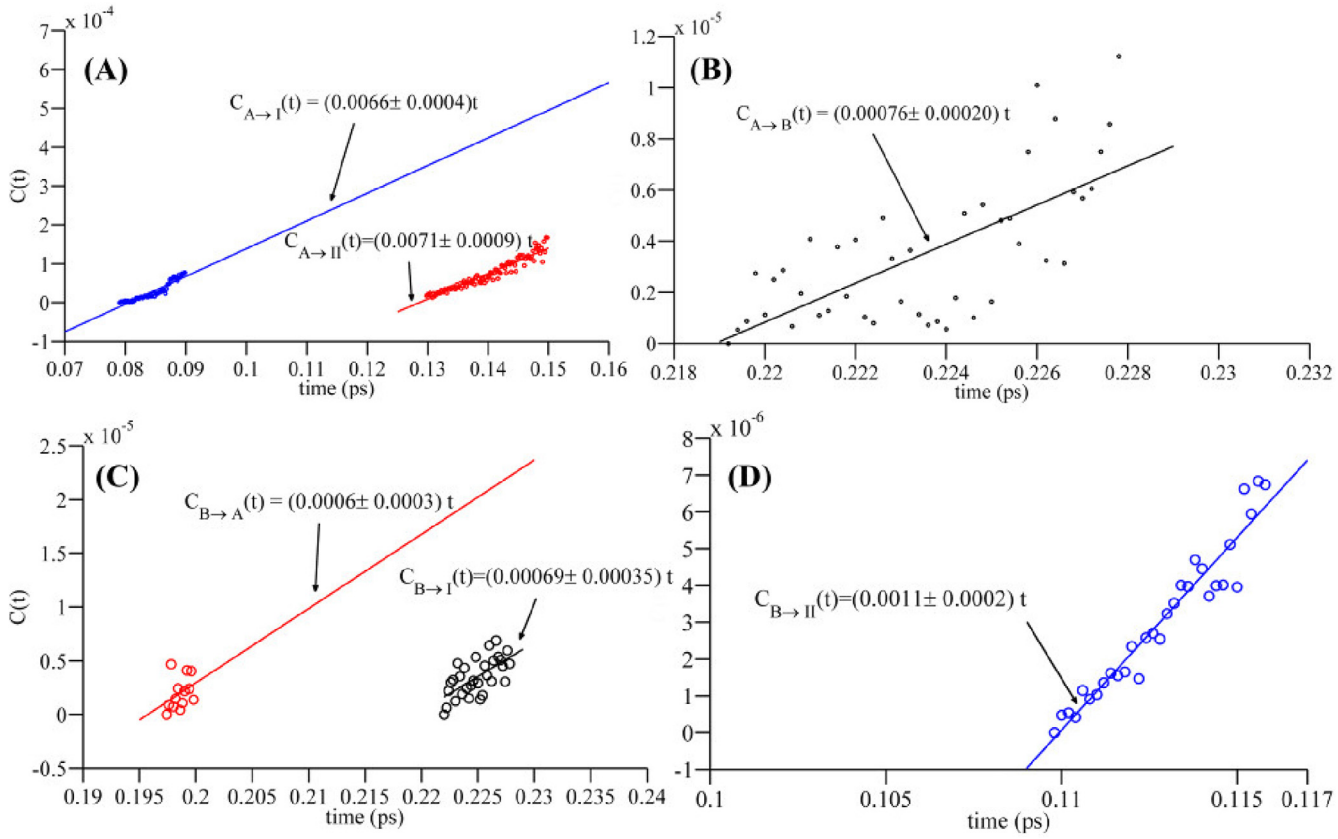

Fig. 5. Time correlation functions for different transitions, as depicted in each plot, for the two dimensional potential energy surface model using re-weighting techniques given by Eq. (14). All simulations are performed at temperature 300 K, mass of particle is 1 amu, total number of trajectories is 5×10^5, starting from different initial conditions of the unbiased simulation in the product region. Time step is 0.001 ps, and the block averages are performed every 1000 steps. The straight fitting lines given by Eq. (10) are also shown.

the calculated and analytical distribution, with a Pearson correlation coefficient of $R = 0.98$.

To compute the time correlation functions, we generated 5×10^5 trajectories, starting from different conditions in the product region. Initial particle positions and velocities for each trajectory were generated using an unbiased simulation at temperature 300 K. Each time that the system visited one of the four possible minimum states, the global best position $\mathbf{q}^{\text{Gbest}}$ was chosen randomly with equal probability between three other minimum positions. While $\mathbf{q}^{\text{Lbest}}$ was updated every time the system visited a new position with lower potential energy. After omitting the part of correlation function corresponding to the transient time, the rate constant is calculated using a least-squares regression of $C(t)$.

Fig. 1 shows, as an illustration, the distribution of configurations as a scatter points in the two-dimensional potential energy surface with contour lines drawn every $0.5k_BT$ step. The positions of four minimum states are also indicated on the figure. Our results show that the system is able to visit all the minimum states, and moreover, the transition from *A* to *B* is obtained via a single channel containing the two intermediate states *I* and *II*.

Fig. 5 presents the time correlations of the transitions $A\to I$, $A\to II$, and $A\to B$ shown in Fig. 5 (A-B), and the transitions $B\to I$, $B\to II$, and $B\to A$ shown in Fig. 5 (C-D). Our results show that the rate constants of the transitions $A\to I$ and $A\to II$ have similar values, as also indicated from Fig. 5 (A) where the fitting curves are almost parallel to each other. The values of rate constants for these two transitions are shown in Table 1 along with their statistical error. The rate constant of the transition $A\to B$ is about 10 times smaller (see Fig. 5 (B) or Table 1), indicating that this transition is slower compare to the transitions $A\to I$ and $A\to II$. Moreover, these results show that states *I* and *II* serve as intermediate states for the transition $A\to B$.

On the other hand, the constant rates of the transitions $B\to A$ and $B\to I$ have comparison values and smaller than the transition $B\to II$, as indicated in Fig. 5 (C-D) and Table 1. This result indicates that the transitions from $B\to A$ use the state *II* as an intermediate metastable state.

The complete data set used for evaluation of the $A\to B$ and $B\to A$ transitions and performing the statistics are shown in Fig. 6A and B, respectively, as unweighted scatter points.

Table 1
Rate constants for the transitions $A\to I$, $A\to II$, $A\to B$, $B\to I$, $B\to II$, and $B\to A$.

Transition	Rate constant (ps^{-1})
$A\to B$	0.00076±0.00020
$A\to I$	0.0066±0.0004
$A\to II$	0.0071±0.0009
$B\to A$	0.00060±0.00030
$B\to I$	0.00069±0.00035
$B\to II$	0.0011±0.0002

4.2. Coarse-grained model

For the coarse-grained model, results of our study show that the system exhibits a folding/unfolding phase transition at $T = 293$ K, and hence, it is considered to be a good test system for comparing the methods. This is also confirmed from our simulations, where a

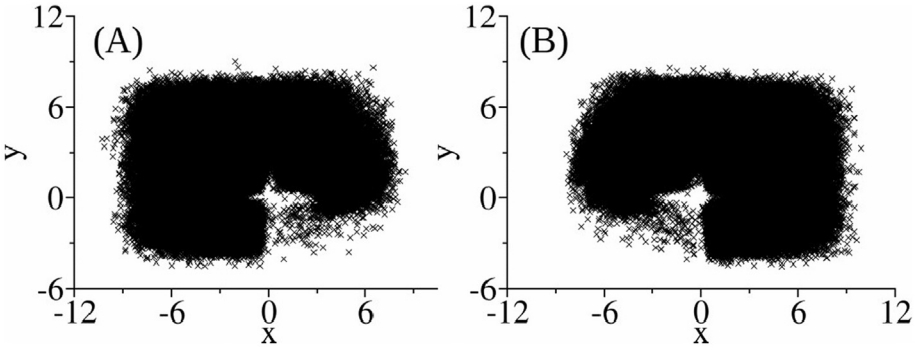

Fig. 6. Unweighted scatter data points used to calculate the time correlation functions of different transitions for the two dimensional potential energy surface model from the simulations at temperature $T = 300$ K. (A) For 5×10^5 trajectories starting from different initial conditions at state *A*. (B) For 5×10^5 trajectories starting from different initial conditions at state *B*.

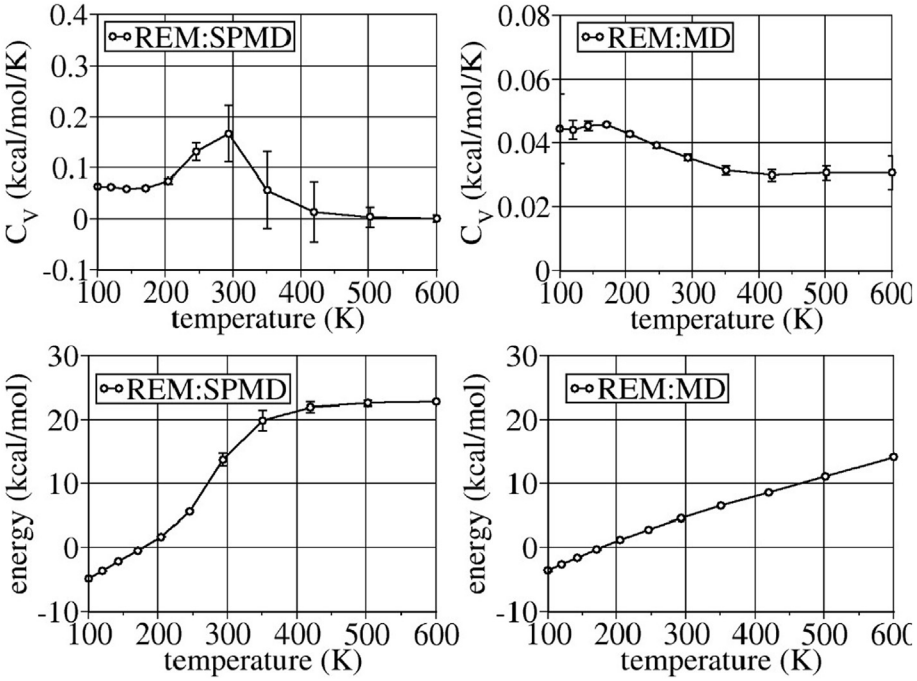

Fig. 7. Total energy (bottom) and specific heat (top) plotted versus temperature for the coarse-grained model of α-helix as obtained by REM:SPMD (left) and REM:MD (right) simulations. WHAM is used to obtain the statistical averages and standard deviations at the desired temperature by analyzing data from all replicas.

discontinuity in internal potential energy and heat capacity is observed at this temperature, as shown in Fig. 7 (left) for α-helix from REM:SPMD simulations. On the other hand, REM:MD simulations fail to identify the transition temperature from folded to unfolded state. Our interpretation of these discrepancies is related on efficiency of each method in minimizing the time for a full round-trip that each replica needs between the two extreme states, which represent replicas with the lowest and highest temperatures. In REM:MD approach, the replicas with lower temperatures ($T < 293$ K) are not able to exchange with those at higher temperatures ($T > 293$ K), and vice-versa. This has in general been observed for the systems with temperature dependent heat capacity [91]. WHAM is used to obtain the statistical averages and standard deviations at the desired temperature by analyzing data from all replicas.

4.3. Atomistic model

4.3.1. Protocol 1

In this protocol, we run MD simulations, separately, for two systems, the α-helix and β-sheet, by coupling each to a single chain of thermostats at temperature 300 K to adjust the temperature of each system during the simulation runs. To assess the convergence of algorithms, we calculated the root mean square deviation (rmsd) according to formula

$$\text{rmsd} = \left(\frac{1}{N} \sum_{i=1}^{N} (\mathbf{r}_i(t) - \mathbf{r}_i(0))^2 \right)^{1/2}$$

where $\mathbf{r}_i(t)$ is the position vector of atom i at time t, and $\mathbf{r}_i(0)$ is the corresponding position vector in reference structure. The sum runs over all N atoms of the structure selected for calculation. The rmsd is measured after removing the overall rotation and translation motions by performing a least-square fitting to reference structure

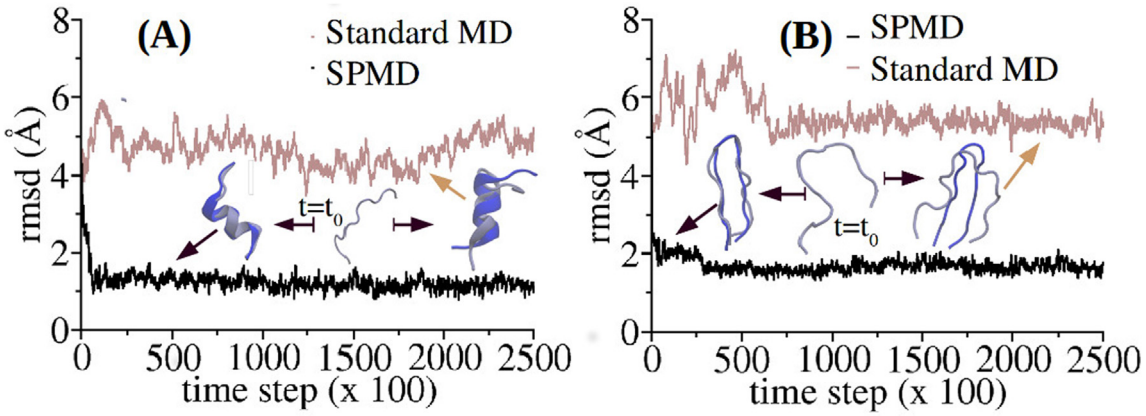

Fig. 8. The rmsd (in Å) of simulation trajectory snapshots from the reference structure for α-helix (A) and β-sheet (B). Inset are shown the 3D overlaps between the reference structure and simulation conformation with the lowest value of rmsd. In addition, the initial structures of our simulations for each system are shown as depicted at $t = t_0$ for (A) α-helix and (B) β-sheet. 3D plots are created using VMD [92].

[3]. We considered, for both, fitting and rmsd calculations, only the backbone atoms. All the calculations were performed using rmsd routine of VMD program [92]. Results of rmsd (in Å) are plotted in Fig. 8. It is apparent from our results that SPMD simulations have lower rmsd compare to standard MD, and this is consistent for both systems. Moreover, it can be seen that convergence (between $0.5 - 1.0$ Å for α-helix and between $1.0 - 2.0$ Å for β-sheet) of the rmsd is obtained in the first 100 ps for SPMD simulation, as presented in Fig. 8. On the other hand, for standard MD simulations the rmsd varies in the range from 4.0 Å to 6.0 Å, and the convergence is about 5–6 times slower compare to SPMD simulations (see also Fig. 8). In addition, we have showed the overlaps between reference structure and the one obtained from each simulation corresponding to the lowest value of rmsd. Plots, shown inset in Fig. 8, are created using visual molecular dynamics (VMD) program [92]. It can be seen that the folded secondary structures, consistent with reference ones, are obtained during SPMD simulations for both systems, in contrast, the results of standard MD runs show that structures with the lowest value of rmsd are significantly different from reference structures. We have also shown the initial structures used in our simulations for each system.

For sake of comparison, we have also performed TMD simulations [60,61] for α-helical and β-sheet structures. The reference structure as determined above are used as target configuration for each system. Here, we used the TMD method as implemented in CHARMM program [62]. Note that in TMD, the holonomic constraints are applied to reduce the root mean square deviation with a preferred target configuration at each MD step. The results of rmsd calculated using SPMD and TMD method, respectively, versus the MD time step are shown graphically in Fig. 9. The quantity d, depicted in Fig. 9, denotes the root mean square increment at each MD step, which also determines the speed of convergence, and hence the slope of the rmsd curves in our plots (see Fig. 9). The rmsd of TMD method is shown for different values of d, and the dynamics are forced to stop when a rmsd of 0.5 Å from the target is reached in all cases. As expected, the target structure is reached faster as the speed d increases for both systems (see also Fig. 9A and B). Interestingly, for the values of d chosen in this study ($d = 0.0001$, 0.0002 and 0.0005) the convergence to the target is comparable in both approaches, TMD and SPMD, in particular for large values of d. It is worth noting that in TMD, the full configuration space is restricted due to the constraints allowing the motion to a restricted subspace of extended configuration space. Moreover, the constraint forces, in general, may not satisfy the restriction that no net virtual work is done by the forces of constraint for any possible virtual displacement, except for the cases when the virtual displacement is in direction perpendicular to the constraint forces. Therefore, the system may be driven out of the equilibrium dynamics, and hence the pulling may have to be really slowly, in practice, depending also on the system, in order to avoid any distortion from equilibrium dynamics.

4.3.2. Protocol 2

In the second protocol, we run replica exchange simulations using both REM:MD and REM:SPMD algorithms with fixed global

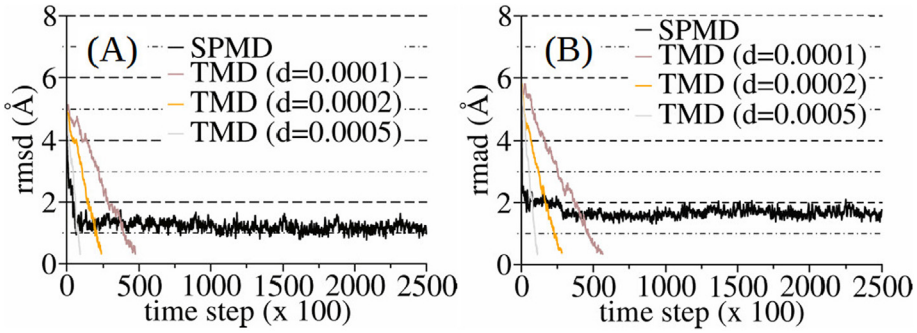

Fig. 9. Comparison of the rmsd from the reference structure (in Å) of simulation trajectory snapshots obtained using SPMD and TMD methods for α-helix (A) and β-sheet (B). The TMD simulations were performed at different speeds characterized by $d = 0.0001$, 0.0002, and 0.0005 [60] as implemented in CHARMM program [62].

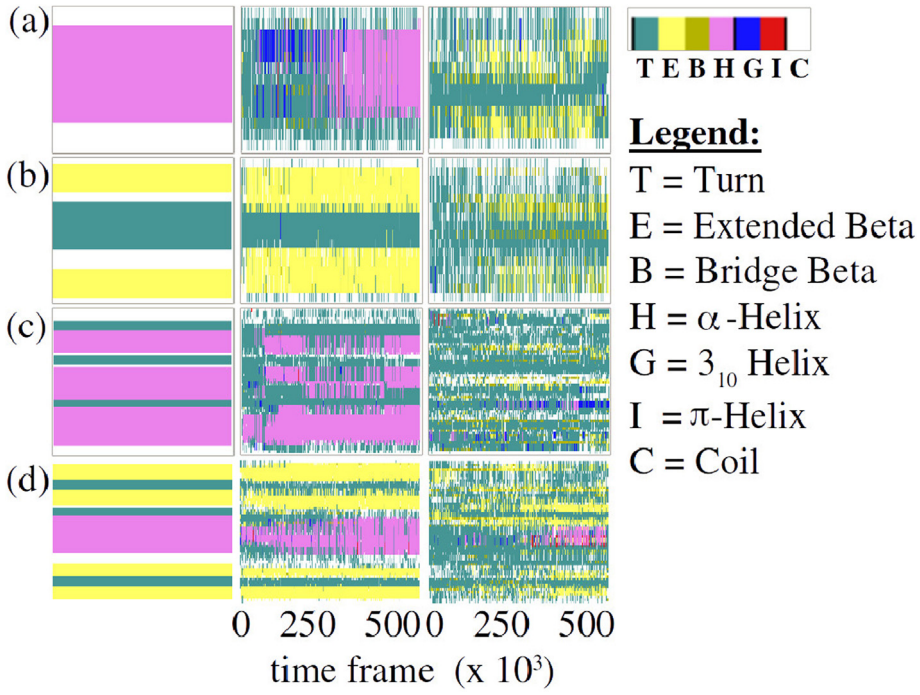

Fig. 10. Secondary structures of the reference structures (left) and of trajectory snapshots obtained from replica exchange simulations using REM:SPMD (middle) and REM:MD (right) approaches. (a) α-Helix; (b) β-sheet; (c) B fragment of protein A (PDB ID 1BDD); (d) C2 fragment of protein G (PDB ID 1FCC). The secondary structures are calculated using STRIDE program [93] implemented in VMD [92]. A color bar of secondary structures is also shown according to structure color assignment in VMD. (For interpretation of the references to color in this figure legend, the reader is referred to the Web version of this article.)

best positions to reference structures. In Fig. 10, we present the secondary structures explored from all replicas visiting thermostat at $T = 300$ K. The results are shown for four systems characterized by different complexity in secondary structures, respectively, α-helix (Fig. 10a), β-sheet (Fig. 10b), B fragment of protein A (Fig. 10c) and C2 fragment of protein G (Fig. 10d). In addition, the secondary structures from the reference coordinates are also shown in Fig. 10 (left) for each system (Fig. 10a-d). The trajectories were analyzed using STRIDE program [93] as implemented in VMD package [92]. It is apparent from our results that after 0.5 ns, during REM:SPMD simulations we obtained the folded state with a secondary structure pattern very similar to the reference structure, which becomes a stable state after 0.5 ns, as shown in Fig. 10a–d (middle). On the other hand, straightforward REM:MD simulations show that there exists a high barrier to folding state which is preventing the system for a transition from unfolded to a folded state in an accessible simulation time scale, as it can be observed by comparing secondary structures of REM:MD simulations with reference structure from Fig. 10a–d (right). These results indicate that REM:SPMD approach is capable of sampling efficiently the local basins and, additionally, enhancing conformational transition sampling. Our results are consistent for all four systems investigated in this work despite the different characteristics in their secondary structures.

To further demonstrate the efficiency of REM:SPMD method, we also calculated the rmsd (in Å) for each simulation using only the trajectory snapshots of all replicas visiting the thermostat at temperature $T = 300$ K, and show the results graphically in Fig. 11. It can be seen that rmsd in REM:SPMD simulations converges to the smallest value observed of 0.87 Å for α-helix, 0.70 Å for β-sheet, 1.51 Å for B fragment of protein A and 1.60 Å for C2 fragment of protein G. Interestingly, on the other hand, in REM:MD simulations we have observed a rmsd stabilized between 4.0 and 6.0 Å for α-helix and β-sheet, and larger than 9.0 Å for B fragment of protein A and C2 fragment of protein G, indicating that the system is probably trapped into some metastable state being unable to reach the folded state in an accessible time scale for simulations we conducted in this study.

In addition, to enhance our understanding of the REM:SPMD approach efficiency, we have created plots of 3D structure overlaps between configurations with the smallest value of rmsd and reference structures for both methods. The graphs are presented for all four systems studied here in Fig. 12. Moreover, we have also shown the initial structures used for each simulation. From our results it is apparent that REM:SPMD out performs REM:MD in that for all systems shown here the obtained folded configurations have the same structure features as native X-ray structure. These results, further indicate that during REM:SPMD simulation the local basins are efficiently sampled, in addition, swarm replicas cooperatively sample more phase space by steering each other across potential energy barriers.

One of the problems in MD simulations of complex molecular systems is the sampling of the phase space [9]. It has been proposed elsewhere [94] an estimation of the simulation length needed to guarantee that ergodic hypothesis is satisfied, by introducing the following quantity:

$$E(t) = \frac{1}{N_{\text{bins}}} \sum_{i=1}^{N_{\text{bins}}} \left(A_i^{(1)}(t) - A_i^{(2)}(t) \right)^2 \tag{18}$$

where $A_i^{(j)}$ is the value of any macroscopic property of the system (e.g., the potential energy) from the j-th trajectory at the bin i, N_{bins} is the total number of histogram bins, and t is the simulation time. If the system is ergodic, then $E(t)$ decays to zero as $1/D\tau$, where D is the generalized diffusion constant and τ is a time scale for self-averaging in the simulation. Moreover, the decay of ergodic measure to zero at long times is a necessary condition for the calculated

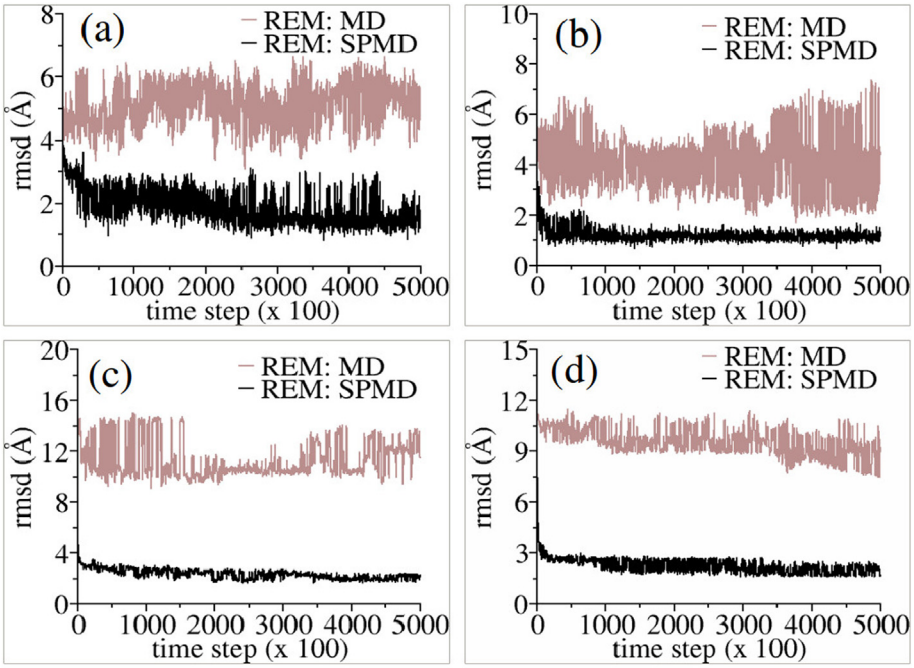

Fig. 11. The rmsd (in Å) of replica exchange trajectory of snapshots from reference structures obtained from REM:SPMD and REM:MD simulations. (a) α-Helix; (b) β-sheet; (c) B fragment of protein A (PDB ID 1BDD); (d) C2 fragment of protein G (PDB ID 1FCC). For each system, the simulations started from the same unfolded conformation.

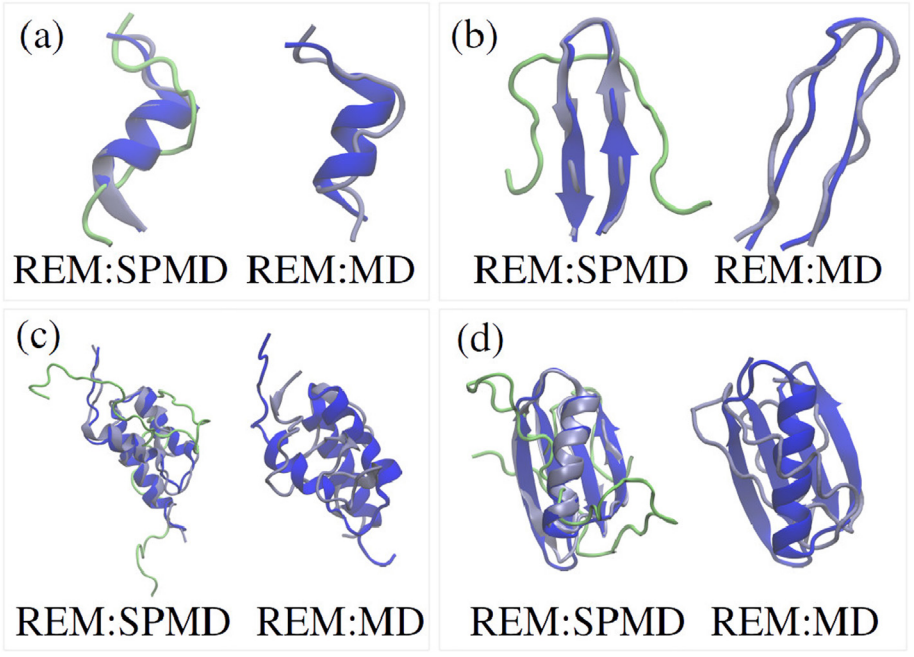

Fig. 12. 3D structure overlaps between configurations from trajectory of snapshots with the lowest value of rmsd (in light blue color) and reference structure (in blue color). In addition, the initial structures of the replica exchange simulations are shown (in green color). The plots are created using VMD [92]. (a) α-Helix; (b) β-sheet; (c) B fragment of protein A (PDB ID 1BDD); (d) C2 fragment of protein G (PDB ID 1FCC). (For interpretation of the references to color in this figure legend, the reader is referred to the Web version of this article.)

average properties to correspond with equilibrium thermodynamic averages. In this work, we calculated the ergodicity measure of the potential energy for the four systems presented here, and show the results graphically in Fig. 13, using both methods, REM:MD and REM:SPMD. In all simulations trajectories started from different initial conditions and completely unfolded states, and $E(t)$ was calculated from the contributions of all replicas. It can be seen that $E(t)$ goes faster to zero in REM:SPMD than in REM:MD; therefore, this is an indication that the sampling in REM:SPMD is more efficient than in REM:MD.

4.3.3. Protocol 3

In the third protocol, we run replica exchange simulations using both REM:MD and REM:SPMD algorithms with global best

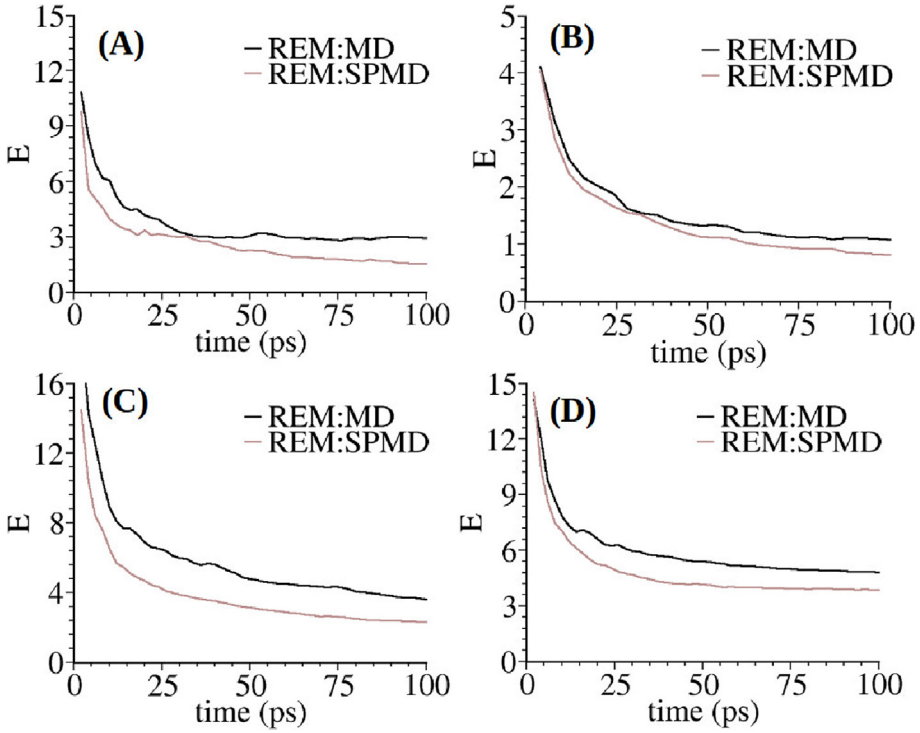

Fig. 13. The potential energy variance between two independent trajectories (see Eq. (18)) as a function of the simulation time obtained from REM:SPMD and REM:MD runs for (a) α-Helix; (b) β-sheet; (c) B fragment of protein A (PDB ID 1BDD); (d) C2 fragment of protein G (PDB ID 1FCC). The data from all replicas are used to construct the histograms of potential energy.

positions updated every time step to the configuration with the lowest value of potential energy among all replicas. Note that this protocol would correspond to a "blind" prediction of the reference folded structure as very recently reported in literature [7]. Here, we run eight replicas associated with eight thermostats at temperatures 280, 300, 320, 340, 360, 380, 400, and 420, respectively. Every replica trajectory was 40 ns long with configurations recorded at every 2 ps. Results are shown graphically in Fig. 14. First, we show the free energy contour map versus the rmsd (Å) and radius of gyration R_g (Å) of the α-helix using REM:SPMD (left) and REM:MD (right) methods, weighted using WHAM at the temperature $T = 300$ K and collected for 320 ns (from all replicas). The rmsd and R_g are both calculated using corresponding routines in VMD [92]. The energy scale is in units of k_BT. The red regions denote areas not visited during the course of simulations. Letter U denotes the unfolded state, F the folded state and M a metastable state. Our results indicate that in REM:SPMD simulations the complete folded state is accessible within simulation time scale presented here, and interestingly, both unfolded and folded states are visited during simulations. On the other hand, as shown in Fig. 14 (top, right), in REM:MD simulations the system is trapped into a metastable state (almost the entire simulation time), which is identified as β-sheet like structure. Importantly, this is also confirmed by further analysis of the secondary structures of trajectory snapshots shown in Fig. 14 (bottom) using both methods for α-helix. It is apparent from our graphs that α-helical structure is quite stable secondary structure in REM:SPMD method, and on the other hand, in REM:MD runs the α-helix is not accessible within this time scale, moreover, it can be seen that β-sheet secondary structure observed in our simulation is confirmed to be a metastable state.

An explanation of the above findings is related with possibility of system getting trapped into some local minimum, as is in the case of REM:MD simulations. This could happen because the high temperature replicas do not swap frequently with the ones at lower temperatures. To show this, we calculated the probability distribution of every replica among the thermostats. Our results indicate that the REM:SPMD simulation performed better on optimizing the distribution of replicas among the thermostats with time, as presented by plots shown in Fig. 15. Clearly, almost flat probability distributions are obtained from REM:SPMD run, and on the other hand in the REM:MD simulation run, the higher temperature replicas experience high barriers on the way to lower temperatures, and vice-versa, decreasing the possibilities for upper and lower temperature replicas to exchange. It is apparent from our test example that REM:SPMD provides a good Monte Carlo sampling method in the temperature space.

It is also worth noting that in all our analysis the global minimum of the potential energy function is assumed to coincide with the structures obtained from X-ray experiments, after optimizing the positions of missing hydrogen atoms. This may create artefacts on the simulations using method introduced here, since, in general, the minimum of the potential energy function is a force field dependent problem and may not necessarily be obtained at the position of the experimental structure coordinates. This is particularly important in the case of "Protocol 1″ and "Protocol 2″, investigated here, where it is assumed that the global best configuration is taken from X-ray structure, and hence it also represents the global minimum of potential energy function. However, we think that in these cases, the global minimum will eventually be one of the so-called here "local best position", and the presence of the third term in Eq. (7) allows efficient sampling of this region of the configuration phase space, as demonstrated above, although it does not represent the target structure in simulation. Therefore, the ability of sampling the local regions as well as being enforced to reach the target configuration makes this method (SPMD) more efficient than the other standard methods discussed here, since

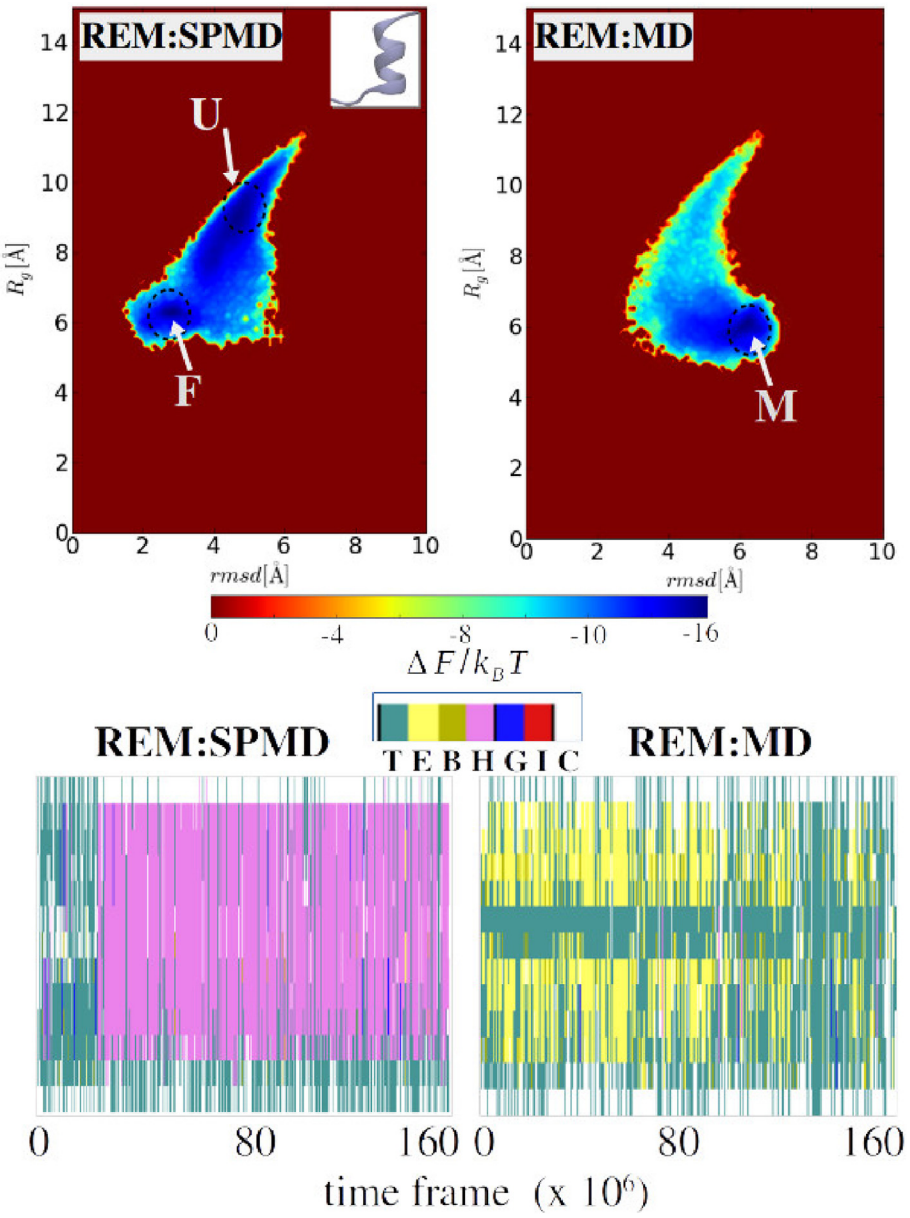

Fig. 14. (Top) Free energy contour map vs the rmsd (Å) and radius of gyration R_g (Å) of the α-helix from REM:SPMD (left) and REM:MD (right) methods, weighted using WHAM at the temperature $T = 300$ K and collected for 320 ns. The energy scale is in units of k_BT. The red regions denote areas not visited during the course of simulations. (Bottom) Secondary structures of trajectory snapshots obtained from replica exchange simulations using REM:SPMD (left) and REM:MD (right) methods for α-helix. The secondary structures are calculated using STRIDE program [93] implemented in VMD [92]. A color bar of secondary structures is also shown according to structure color assignment in VMD. (For interpretation of the references to color in this figure legend, the reader is referred to the Web version of this article.)

SPMD allows in this way sampling all directional degrees of freedom of the system.

In the case of "Protocol 3″, the global minimum is not assumed to be known *a priory*, and these artefacts are no longer present. However, in our analysis above there may be expected some discrepancies when comparisons are made with X-ray structures, which may not characterize the structure coordinates of the global minimum of potential energy function. This can also be supported by the fact that α-helical structure is only a part of the complete X-ray structure, as such it does not represent an experimental configuration in itself. Therefore, the rmsd and/or R_g values of α-helix may not be the same with those values of α-helix as a part of protein, as predicted by X-ray experiment, in particular, the terminal regions. Nevertheless, our results are interesting, because the folded helical and unfolded structures are regularly observed during the simulation run.

It is interesting to note that the method introduced here may also be efficient in studying large scale conformation transitions in proteins in time scales that are not accessible using standard MD simulations, in particular, when the structures of these conformations are known, similar to some applications of TMD method [61]. These could also include cases when more than one target structure is known for the system. For instance, using the approach of the 2-D potential energy surface model, where the switching between the target configurations can be performed during the simulations, in order to setup $\mathbf{q}^{\text{Gbest}}$, with equal probability each time that one of the target configurations is observed. In addition, the form of Eq. (7) allows accelerating the transitions of barriers along the specified

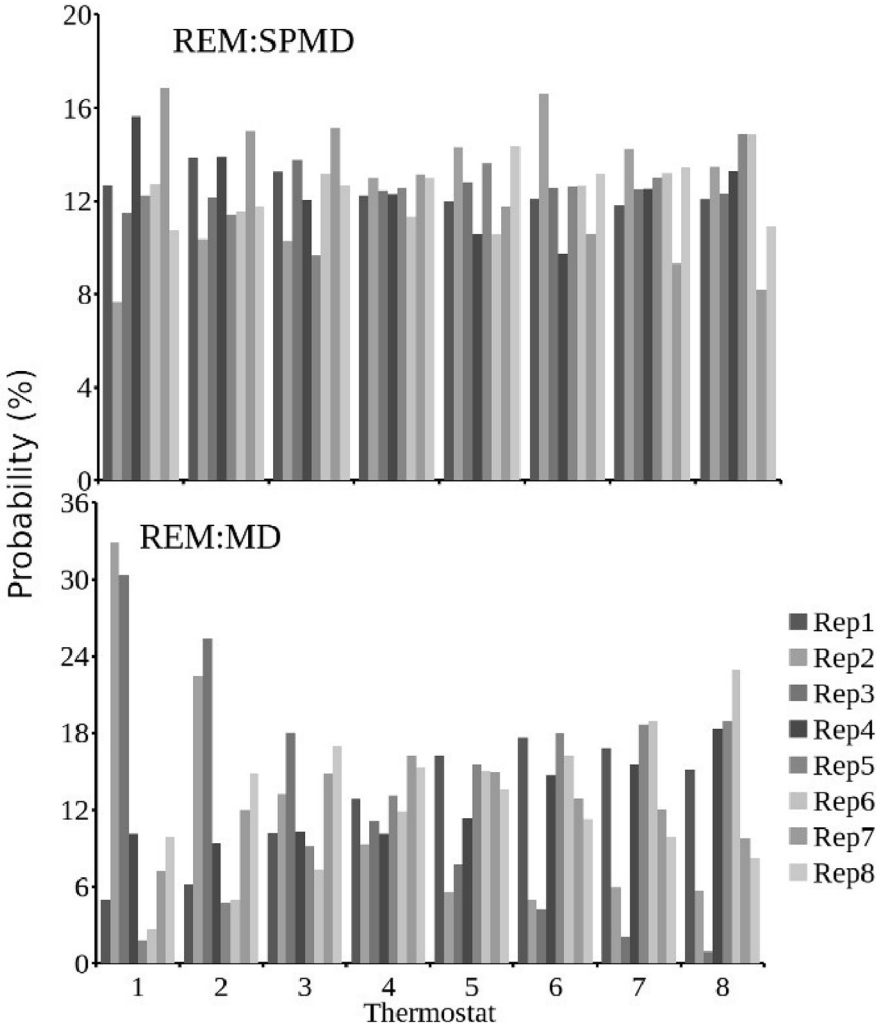

Fig. 15. Probability of finding every replica at a thermostat position (in percentage) during the course of simulations for REM:SPMD run (left) and REM:MD run (right).

reaction coordinates for an efficient construction of free energy landscape in the reduced phase space of essential degrees of freedom [95].

A limitation of the method discussed here includes the study of time correlations between different conformations, which are separated by a large number of barriers, in particular for rough energy landscapes. In this case, to avoid the limitations, we will have to tune the parameters involved on the equations of motion, such as γ_1 and γ_2, which will in practice adjust the speed of the convergence towards the target structures and the smoothness of energy landscape. During the fast transitions between the conformations the long time scale kinetics may be recovered, and so do the time correlations between the low frequency modes, however, the short-time correlations between the high frequency modes can not be recovered because of the lack of the information obtained from the dynamics of these modes. Therefore, theoretically, one have to adjust these discrepancies by tuning the parameters γ_1 and γ_2.

Furthermore, if the simulations are faster accelerated to overcome energetic barriers ignoring in this way some ranges of frequency motions, which happens for high values of γ_2, in particular, then U_{bias} term will take a wide range of values (eventually, some will have large values), and hence, the re-weighted averages will be dominated by a few terms corresponding to the structures with high values of U_{bias} assuming that we have a finite number of samples from the simulation. This can be considered as a statistical pitfall on performing WHAM analysis, which results in reduction of data entry from MD simulations, and hence high degree of acceleration may yield a poor statistical accuracy on calculations of statistical errors, in particular. To avoid this, one can think of varying the degree of acceleration among the replicas as well. In our approach this can be easily introduced, as also been done in our study of coarse-grained potential model, by introducing temperature dependent constants, such as $\gamma_1 = \gamma_1^{(0)}/k_BT$ and $\gamma_2 = \gamma_2^{(0)}/k_BT$, with $\gamma_1^{(0)}$ and $\gamma_2^{(0)}$ being two adjustable parameters. Moreover, to reduce the energetic noise due to the statistical inefficiency, more sophisticated methods can also be considered, for example, by calculation the Boltzmann's factors as Maclaurin series of the boost potential U_{bias}, which has already been discussed in the literature [96].

5. Conclusions

In this study we presented a new approach based on swarm particle-like dynamics, characterizing an augmented dynamical system, which can be used in molecular dynamics simulation to enhance the transition path sampling in phase space, by improving the efficiency of local basins searching and increasing the barrier

crossing rate.

The main advantages of our method is that does not require *a priory* knowledge of the energy distribution among the thermostats as function of temperature when applied to standard replica exchange method, and in addition does not require any knowledge of potential energy landscape.

The new method presented in this study out performed the standard replica exchange approach on capability of folding faster the proteins to minimum energy state for all systems investigated here. In addition, the new method (REM:SPMD) was capable of optimizing the probability distribution of replicas among the thermostats, minimizing in this way the time for a full round-trip from the lowest to highest temperature.

Our results indicated that in less than 0.5 ns we could fold proteins of 46 and 56 amino acids to native X-ray structure starting from a completely unfolded state with the new approach presented in this study, assuming that native folded structure is known. Furthermore, in employing protocol three we performed a blind prediction of the folded state of the α-helix structure. Our results indicated that REM:SPMD method was able to predict the folded structure within simulation time of 40 ns with a minimum rmsd less than 2.0 Å.

Our method shown in this study demonstrated comparable results with more standard methods shown in the literature, such as TMD approach [60,61].

In this study, we showed that calculations of the thermodynamic averages can be solved by enhancement of the conformational sampling using a statistical ensemble corresponding to *nonphysical* dynamical system. Then, using proper re-weighting technique, we showed how to recover the Boltzmann weights of physical dynamical system. Furthermore, we demonstrated for a two dimensional surface that it is possible to exactly calculate the kinetic properties of the *physical* system undergoing Nosé-Hoover dynamics. Moreover, we showed stability of the algorithm in terms of energy conservation.

In addition, we think that the method can be combined with already existing methods used to enhance the conformational search to further improve the sampling efficiency, particularly, in temperature phase space of replica exchange approaches [73–77]. Moreover, the approach introduced here can be used to allow accelerating the transitions of barriers along the specified reaction coordinates for an efficient construction of free energy landscape in the reduced phase space of essential degrees of freedom.

Acknowledgments

The author would like to thank the International Balkan University for the support.

Appendix A. Supplementary data

Supplementary data related to this article can be found at https://doi.org/10.1016/j.jmgm.2018.02.008.

References

[1] M. Karplus, J.A. McCammon, Molecular dynamics simulations of biomolecules, Nat. Struct. Biol. 9 (9) (2002) 646–652 with corrigenda in Nat. Struct. Biol. 9(10),788 (2002).
[2] W. van Gunsteren, D. Bakowies, R. Baron, I. Chandrasekhar, M. Christen, X. Daura, P. Gee, Biomolecular modeling: goals, problems, perspectives, Angew. Chem. Int. Ed. 45 (25) (2006) 4064–4092.
[3] A. Amadei, A.B.M. Linssen, H.J.C. Berendsen, Essential dynamics of proteins, Proteins Struct. Funct. Genet. 17 (1993) 412–425.
[4] J. Rogal, P.G. Bolhuis, Multiple state transition path sampling, J. Chem. Phys. 129 (2008), 224107.
[5] P.G. Bolhuis, D. Chandler, C. Dellago, P.L. Geissler, Transition path sampling: throwing ropes over rough mountain passes, in the dark, Annu. Rev. Phys. Chem. 53 (2002) 291–318.
[6] S.L. Seyler, O. Beckstein, Sampling large conformational transitions: adenylate kinase as a testing ground, Mol. Simulat. 40 (10–11) (2014) 855–877.
[7] A. Perez, J.A. Morrone, E. Brini, J.L. MacCallum, K.A. Dill, Blind protein structure prediction using accelerated free-energy simulations, Sci. Adv. 2 (2016) e1601274.
[8] R. Palmer, Broken ergodicity, Adv. Phys. 32 (1982) 669–735.
[9] J.B. Clarage, T. Romo, B.K. Andrews, B.M. Pettitt, G.N.J. Phillips, A sampling problem in molecular dynamics simulations of macromolecules, Proc. Natl. Acad. Sci. U.S.A. 92 (1995) 3288–3292.
[10] G. Ciccotti, E. Vanden-Eijnden, The trees and the forest. Aims and objectives of molecular dynamics simulations, Eur. Phys. J. Spec. Top. 224 (2015) 2515–2518.
[11] M.K. Transtrum, B.B. Machta, K.S. Brown, B.C. Daniels, C.R. Myers, J.P. Sethna, Perspective: sloppiness and emergent theories in physics, biology, and beyond, J. Chem. Phys. 143 (2015) 010901–010913.
[12] A. Piela, J. Kostrowicki, H.A. Scheraga, The multiple-minima problem in the conformational analysis of molecules. deformation of the potential energy hypersurface by the diffusion equation method, J. Phys. Chem. 93 (1989) 3339–3346.
[13] T. Huber, A.E. Torda, W.F. van Gunsteren, Structure optimization combining soft-core interaction functions, the diffusion equation method, and molecular dynamics, J. Phys. Chem. A 101 (1997) 5926–5930.
[14] A. Laio, M. Parrinello, Escaping free-energy minima, Proc. Natl. Acad. Sci. U.S.A. 99 (2002) 12562–12566.
[15] D. Hamelberg, J. Mongan, J. McCammon, Accelerated molecular dynamics: a promising and efficient simulation method for biomolecules, J. Chem. Phys. 120 (24) (2004) 11919–11929.
[16] K. Srinivasaraghavan, M. Zacharias, Enhanced sampling of peptide and protein conformations using replica exchange simulations with a peptide backbone biasing potential, Proteins: Struct., Funct., Bioinf. 66 (2007) 697–706.
[17] H. Grubmüller, Predicting slow structural transitions in macromolecular systems: conformational flooding, Phys. Rev. E 52 (1995) 2893–2906.
[18] S. Wells, S. Menor, B. Hespenheide, M. Thorpe, Constrained geometric simulation of diffusive motion in proteins, Phys. Biol. 2 (4) (2005) S127–S136.
[19] I. Andricioaei, J.E. Straub, On Monte Carlo and molecular dynamics methods inspired by Tsallis statistics: methodology, optimization, and application to atomic clusters, J. Chem. Phys. 107 (21) (1997) 9117–9124.
[20] J.S. Wang, R.H. Swendsen, Replica Monte Carlo simulation of spin glasses, Phys. Rev. Lett. 57 (1986) 2607–2609.
[21] D.D. Frantz, D.L. Freeman, J.D. Doll, Reducing quasiergodic behavior in Monte Carlo simulations by jwalking: applications to atomic clusters, J. Chem. Phys. 93 (1990) 2769.
[22] E. Marinari, G. Parisi, Simulated tempering: a new Monte Carlo scheme, Europhys. Lett. 19 (1992) 451.
[23] B.A. Berg, T. Neuhaus, Multicanonical ensemble: a new approach to simulate first-order phase transitions, Phys. Rev. Lett. 68 (1992) 9–12.
[24] D.J. Earl, M.W. Deem, Parallel tempering: Theory, applications, and new perspectives, Phys. Chem. Chem. Phys. 7 (2005) 3910.
[25] Y. Okamoto, Generalized-ensemble algorithms: enhanced sampling techniques for Monte Carlo and molecular dynamics simulations, J. Mol. Graph. Model. 22 (2004) 425–439.
[26] T. Huber, W.F. van Gunsteren, SWARM-MD: searching conformational space by cooperative molecular dynamics, J. Phys. Chem. A 102 (1998) 5937–5943.
[27] H. Kamberaj, Conformational sampling enhancement of replica exchange molecular dynamics simulations using swarm particle intelligence, J. Chem. Phys. 143 (2015) 124105–124108 (hkamberajibu.wikidot.com/rexmd).
[28] K.K. Burusco, N.J. Bruce, I. Alibay, R.A. Bryce, Free energy calculations using a swarm-enhanced sampling molecular dynamics approach, Chem. Phys. Chem. 16 (2015) 3233–3241.
[29] Y. Ueda, H. Taketomi, N. Go, Studies on protein folding, unfolding, and fluctuations by computer simulation. II. A three-dimensional lattice model of lysozyme, Biopolymers 17 (1978) 1531–1548.
[30] J.A. McCammon, S.H. Northrup, M. Karplus, R.M. Levy, Helix-coil transitions in a simple polypeptide model, Biopolymers 19 (1980) 2033–2045.
[31] I. Bahar, R.L. Jernigan, Inter-residue potentials in globular proteins and the dominance of highly specific hydrophilic interactions at close separation, J. Mol. Biol. 266 (1997) 195–214.
[32] A. Irbäck, F. Sjunnesson, S. Wallin, Three-helix-bundle protein in a ramachandran model, Proc. Natl. Acad. Sci. U.S.A. 97 (2000) 13614–13618.
[33] A.V. Smith, C.K. Hall, A-helix formation: discontinuous molecular dynamics on an intermediate resolution model, Proteins 44 (2001) 344–360.
[34] A.V. Smith, C.K. Hall, Assembly of a tetrameric alpha-helical bundle: computer simulations on an intermediate-resolution protein model, Proteins 44 (2001) 376–391.
[35] S. Oldziej, A. Liwo, C. Czaplewski, J. Pillardy, H.A. Scheraga, Optimization of the UNRES force field by hierarchical design of the potential-energy landscape. 2. Off-lattice tests of the method with single proteins, J. Phys. Chem. B 108 (2004) 16934–16949.
[36] V. Tozzini, Coarse-grained models for proteins, Curr. Opin. Struc. Biol. 15 (2005) 144–150.
[37] V. Tozzini, J. McCammon, A coarse grained model for the dynamics of the early stages of the binding mechanism of hiv-1 protease, Chem. Phys. Lett. 413 (2005) 123–128.

[38] V. Tozzini, W. Rocchia, J.A. McCammon, Mapping all-atom models onto one-based coarse-grained models: general properties and applications to a minimal polypeptide model, J. Chem. Theory Comput. 2 (3) (2006) 667–673.
[39] O.F. Lange, H. Grubmüller, Collective Langevin dynamics of conformational motions in proteins, J. Chem. Phys. 124 (21) (2006), 214903.
[40] M. Stepanova, Dynamics of essential collective motions in proteins: theory, Phys. Rev. E 76 (2007), 051918.
[41] H. Kamberaj, A theoretical model for the collective motion of proteins by means of principal component analysis, Open Phys. 9 (1) (2011) 96–109.
[42] E. Lyman, F.M. Ytreberg, D.M. Zuckerman, Resolution exchange simulation, Phys. Rev. Lett. 96 (2006), 028105.
[43] P. Liu, G.A. Voth, Smart resolution replica exchange: an efficient algorithm for exploring complex energy landscapes, J. Chem. Phys. 126 (4) (2007), 045106–6.
[44] H. Kamberaj, A. van der Vaart, Multiple scaling replica exchange for the conformational sampling of biomolecules in explicit water, J. Chem. Phys. 127 (2007) 234102–234107.
[45] S. Jang, E. Kim, Y. Pak, All-atom level direct folding simulation of a miniprotein, J. Chem. Phys. 128 (2008), 105102.
[46] M. Fajer, D. Hamelberg, J.A. McCammon, Replica-exchange accelerated molecular dynamics (rexamd) applied to thermodynamic integration, J. Chem. Theory Comput. 4 (2008) 1565–1569.
[47] A. Karolak, A. van der Vaart, Importance of local interactions for the stability of inhibitory helix 1 of Ets-1 in the apo state, Biophys. Chem. 165–166 (3) (2012) 74–78.
[48] J.D. Chodera, W.C. Swope, J.W. Pitera, C. Seok, K.A. Dill, Use of the weighted histogram analysis method for the analysis of simulated and parallel tempering simulations, J. Chem. Theory Comput. 3 (2007) 26–41.
[49] M.S. Friedrichs, P. Eastman, V. Vaidyanathan, M. Houston, S. Legrand, A.L. Beberg, D.L. Ensign, C.M. Bruns, V.S. Pande, Accelerating molecular dynamics simulation on graphics processing units, J. Comput. Chem. 30 (2009) 864–872.
[50] R.O. Dror, D.H. Arlow, P. Maragakis, T.J. Mildorf, A.C. Pan, H. Xu, D.W. Borhani, Activation mechanism of the β2-adrenergic receptor, Proc. Natl. Acad. Sci. U.S.A. 108 (2011) 18684–18689.
[51] M.E. Tuckerman, B.J. Berne, G.J. Martyna, Reversible multiple time scale molecular dynamics, J. Chem. Phys. 97 (3) (1992) 1990.
[52] M.E. Tuckerman, G.J. Martyna, Understanding modern molecular dynamics: techniques and applications, J. Phys. Chem. B 104 (2000) 159–178.
[53] P. Minary, M.E. Tuckerman, G.J. Martyna, Long time molecular dynamics for enhanced conformational sampling in bimolecular systems, Phys. Rev. Lett. 93 (2004) (150201-4).
[54] T. Schlick, Molecular Modeling and Simulation, second ed., Springer, New York, NY, 2010.
[55] S. Nosé, A unified formulation of the constant temperature molecular dynamics methods, J. Chem. Phys. 81 (1984) 511–519.
[56] E. Gallicchio, M. Andrec, A.K. Felts, R.M. Levy, Temperature weighted histogram analysis method, replica exchange, and transition paths, J. Phys. Chem. B 109 (2005) 6722–6731.
[57] K.A. Dill, K.M. Fiebig, H.S. Chan, Cooperativity in protein-folding kinetics, Proc. Natl. Acad. Sci. U.S.A. 90 (1993) 1942–1946.
[58] A.E. Garcia, J.N. Onuchic, Folding a protein in a computer: an atomic description of the folding/unfolding of protein A, Proc. Natl. Acad. Sci. U.S.A. 100 (2003) 13898–13903.
[59] R. Zhou, Free energy landscape of protein folding in water: explicit vs. implicit solvent, Proteins: Struct., Funct., Bioinf. 53 (2) (2003) 148–161.
[60] J. Schlitter, M. Engels, P. Krüger, E. Jacoby, A. Wollmer, Targeted molecular dynamics simulation of conformational change-application to the T R transition in insulin, Mol. Simulat. 10 (2–6) (1993) 291–308.
[61] A. van der Vaart, M. Karplus, Simulation of conformational transitions by the restricted perturbation-targeted molecular dynamics method, J. Chem. Phys. 122 (2005), 114903.
[62] B.R. Brooks, R.E. Bruccoleri, B.D. Olafson, D.J. States, S. Swaminathan, M. Karplus, Charmm: a program for macromolecular energy, minimization, and dynamics calculations, J. Comput. Chem. 4 (2) (1983) 187–217.
[63] Y. Miao, F. Feixas, C. Eun, J.A. McCammon, Accelerated molecular dynamics simulations of protein folding, J. Comput. Chem. 36 (2015) 1536–1549.
[64] W. Hoover, Canonical dynamics: equilibrium phase-space distributions, Phys. Rev. A 31 (1985) 1695–1697.
[65] G.J. Martyna, M.L. Klein, M. Tuckerman, Nosé-hoover chains: the canonical ensemble via continuous dynamics, J. Chem. Phys. 97 (1992) 2635.
[66] A.M. Ferrenberg, R.H. Swendsen, Optimized Monte Carlo data analysis, Phys. Rev. Lett. 63 (1989) 1195–1198.
[67] Y. Sugita, Y. Okamoto, Replica-exchange molecular dynamics method for protein folding, Chem. Phys. Lett. 314 (1999) 141–151.
[68] G. Hummer, A. Szabo, Free energy profiles from single-molecule pulling experiments, Proc. Natl. Acad. Sci. U.S.A. 107 (50) (2010) 21441–21446.
[69] J. Kim, J.E. Straub, Optimal replica exchange method combined with Tsallis weight sampling, J. Chem. Phys. 130 (2009), 144114–11.
[70] G.M. Torrie, J.P. Valleau, Monte Carlo free energy estimates using non-boltzmann sampling: application to the sub-critical lennard-jones fluid, Chem. Phys. Lett. 28 (1974) 578–581.
[71] G.M. Torrie, J.P. Valleau, Nonphysical sampling distributions in Monte-Carlo free-energy estimation: umbrella sampling, J. Comput. Phys. 23 (2) (1977) 187–199.
[72] H. Lu, B. Isralewitz, A. Krammer, V. Vogel, K. Schulten, Unfolding of titin immunoglobulin domains by steered molecular dynamics simulation, Biophys. J. 75 (1998) 662–671.
[73] N. Rathore, M. Chopra, J.J. de Pablo, Optimal allocation of replicas in parallel tempering simulations, J. Chem. Phys. 122 (2005), 024111.
[74] A. Kone, D.A. Kofke, Selection of temperature intervals for parallel-tempering simulations, J. Chem. Phys. 122 (2005), 206101.
[75] S. Trebst, D.A. Huse, M. Troyer, Optimizing the ensemble for equilibrium in broad-histogram Monte Carlo, Phys. Rev. E 70 (2004), 046701.
[76] H.G. Katzgraber, S. Trebst, D.A. Huse, M. Troyer, Feedback-optimized parallel tempering Monte Carlo, J. Stat. Mech. 2006 (03) (2006). P03018.
[77] S. Trebst, M. Troyer, U.H.E. Hansmann, Optimized parallel tempering simulations of proteins, J. Chem. Phys. 124 (2006), 174903.
[78] J. MacFadyen, J. Wereszczynski, I. Andricioaei, Directionally negative friction: a method for enhanced sampling of rare event kinetics, J. Chem. Phys. 128 (2008) 114112–114119.
[79] J. MacDadyen, I. Andricioaei, A skewed-momenta method to efficiency generate conformational transition trajectories, J. Chem. Phys. 123 (2005), 074107.
[80] P. Bolhuis, D. Chandler, C. Dellago, P. Geissler, Transition path sampling: throwing ropes over rough mountain passes, in the dark, Annu. Rev. Phys. Chem. 53 (2002) 291–318.
[81] C. Jarzynski, Nonequilibrium equality for free energy differences, Phys. Rev. Lett. 78 (1997) 2690–2693.
[82] A. Wlodawer, J. Walter, R. Huber, L. Sjolin, Structure of bovine pancreatic trypsin inhibitor. results of joint neutron and x-ray refinement of crystal form ii, J. Mol. Biol. 180 (1984) 301–329.
[83] T. Lazaridis, M. Karplus, Effective energy function for proteins in solution, Proteins 35 (1999) 133–152.
[84] H. Gouda, H. Torigoe, A. Saito, M. Sato, Y. Arata, I. Shimada, Three-dimensional solution structure of the b domain of staphylococcal protein a: comparisons of the solution and crystal structures, Biochemistry 31 (1992) 9665–9672.
[85] A.E. Sauer-Erikson, G.J. Kleywegt, M. Uhlen, T.A. Jones, Crystal structure of the c2 fragment of streptococcal protein g in complex with the fc domain of human igg, Structure 3 (1995) 265–278.
[86] S. Jo, T. Kim, V.G. Lyer, W. Im, Charmm-gui: a web-based graphical user interface for charmm, J. Comput. Chem. 29 (2008) 1859–1865.
[87] L. Wesson, D. Eisenberg, Atomic solvation parameters applied to molecular dynamics of proteins in solution, Protein Sci. 1 (1992) 227–235.
[88] G.J. Martyna, M.E. Tuckerman, D.J. Tobias, M.L. Klein, Explicit reversible integrators for extended systems dynamics, Mol. Phys. 87 (1996) 1117–1157.
[89] G. Lamoureux, B. Roux, Modelling induced polarization with classical drude oscillators: Theory and molecular dynamics simulation algorithm, J. Chem. Phys. 119 (2003) 3025–3039.
[90] J. Ryckaert, G. Ciccotti, H. Berendsen, Numerical integration of the cartesian equations of motion of a system with constraints: molecular dynamics of n-alkanes, J. Comput. Chem. 23 (1977) 327–341.
[91] H. Kamberaj, A. van der Vaart, An optimised replica exchange method for molecular dynamics simulations, J. Chem. Phys. 130 (2009), 074904.
[92] W. Humphrey, A. Dalke, K. Schulten, Vmd - visual molecular dynamics, J. Mol. Graph. 14 (1996) 33–38.
[93] D. Frishman, P. Argos, Knowledge-based secondary structure assignment, Proteins Struct. Funct. Genet. 23 (1995) 566–579.
[94] D. Thirumalai, R.D. Mountain, T.R. Kirkpatrick, Ergodic behaviour in supercooled liquids and glasses, Phys. Rev. A 39 (1989) 3563–3574.
[95] D.J. Wales, Perspective: insight into reaction coordinates and dynamics from the potential energy landscape, J. Chem. Phys. 142 (2015) 130901.
[96] Y. Miao, F. Feixas, C. Eun, J.A. McCammon, Accelerated molecular dynamics simulations of protein folding, J. Comput. Chem. 36 (2015) 1536–1549.